Major sources of North Atlantic Deep Water in the subpolar North Atlantic from Lagrangian analyses in a high–resolution ocean model

Jörg Fröhle[1,2,*], Patricia V. K. Handmann[1,*], and Arne Biastoch[1,2]

[*]These authors have contributed equally to this work and share first authorship
[1]GEOMAR Helmholtz Centre for Ocean Research, Kiel, Germany
[2]Christian-Albrechts-Universität zu Kiel, Kiel, Germany

Correspondence: Jörg Fröhle(jfroehle@geomar.de), Patricia Handmann (phandmann@geomar.de)

Abstract. North Atlantic Deep Water (NADW) is a crucial component of the Atlantic Meridional Overturning Circulation and, therefore, is an important factor of the climate system. In order to estimate the mean relative contributions, sources and pathways of the three different deep water mass components (namely Labrador Sea Water, Northeast Atlantic Deep Water and Denmark Strait Overflow Water) at the southern exit of the Labrador Sea, Lagrangian particle experiments were performed. The particles were seeded according to the strength of the velocity field along the $53°N$ section and computed 40 years backward in time in the three-dimensional velocity and hydrography field. Water masses were defined within the model output in the central Labrador Sea and the subpolar North Atlantic. The resulting transport pathways, their sources and corresponding transit time scales were inferred. Our experiments show that the majority of NADW passing $53°N$ is associated with diapycnal mass flux, accounting for $14.3\ Sv$ (48%), where $6.2\ Sv$ originate from the Labrador Sea, compared to $4.7\ Sv$ from the Irminger Sea. The second largest contribution originates from the mixed layer with $7.2\ Sv$ (24%), where the Labrador Sea contribution ($5.9\ Sv$) dominates over the Irminger Sea contribution ($1.0\ Sv$). Another $5.7\ Sv$ (19%) of NADW cross the Greenland–Scotland Ridge within the NADW density class, where about $2/3$ pass Denmark Strait, while $1/3$ cross the Iceland Scotland Ridge. The NADW exported at $53°N$ is hence dominated by entrainment through diapycnal mass flux and the mixed layer origin in the Labrador Sea.

1 Introduction

Water mass transformation from the upper to the lower Atlantic Meridional Overturning Circulation (AMOC) component associated with deep convective mixing (Lab Sea Group, 1998; Marshall and Schott, 1999) and diapycnal mixing (Straneo, 2006; Katsman et al., 2018) is occurring in the highly complex region of the subpolar North Atlantic (SPNA). The associated density increase eventually results in a net downwelling of upper AMOC water (Johnson et al., 2019) and thereby the formation of deep and intermediate water (Rhein et al., 2011). These water masses are then transported southward through the Deep Western Boundary Current (DWBC) (Dickson and Brown, 1994; Molinari et al., 1998) as well as the interior as part of the deep AMOC branch (Bower et al., 2009). Water mass properties of North Atlantic Deep Water (NADW) are largely imprinted within the SPNA and the Nordic Seas, and mostly maintained farther south (Haine et al., 2008).

At $53°N$, the southern exit of the Labrador Sea, all three components of the NADW are present in the DWBC. The shallowest component, named Labrador Sea Water (LSW), is thought to be majorly formed through deep convective mixing in the Labrador Sea (Yashayaev and Loder, 2016). This water mass is regularly ventilated in winter and is defined as a low potential vorticity water mass with conservative temperatures below $4°C$ and densities between $27.70 - 28.10\ kg\ m^{-3}$ in neutral density (γ_n), $27.68 - 27.80\ kg\ m^{-3}$ in potential density (σ_0) and $36.50 - 36.94\ kg\ m^{-3}$ in potential density relative to $2,000\ m$ (σ_2). The first lower NADW (lNADW) component is the Northeast Atlantic Deep Water (NEADW) or Iceland–Scotland Overflow Water (ISOW) originating at the overflows of the Iceland–Scotland Ridge (ISR) (Hansen and Østerhus, 2000; Østerhus et al., 2001; Jochumsen et al., 2015). This water mass is featuring conservative temperatures between $2.2 - 3.3°C$ and high absolute salinities of $> 34.95\ g\ kg^{-1}$ with γ_n between $28.00 - 28.15\ kg\ m^{-3}$, $27.80 - 27.88\ kg\ m^{-3}$ in σ_0 and $36.94 - 36.98\ kg\ m^{-3}$ in σ_2. NEADW appears as a salinity maximum at depth in the hydrography of $53°N$ below the LSW component. The deepest lNADW component is the Denmark Strait Overflow Water (DSOW) originating at the overflow sills of Denmark Strait (DS) between Greenland and Iceland with densities $\gamma_n > 28.15\ kg\ m^{-3}$, $\sigma_0 > 27.88\ kg\ m^{-3}$ and $\sigma_2 > 36.98\ kg\ m^{-3}$ (Pickart et al., 1997; Schott et al., 2006; Liu and Tanhua, 2021). The origins of the multi-annual transport variability of these lNADW components found at $53°N$ still remain a subject of discussion (Zantopp et al., 2017).

From the observed mid–depth flow field (Palter et al., 2016; Fischer et al., 2018), the spreading path of the mid–depth water masses is known as follows: The ISOW flows along the eastern flank of the Reykjanes Ridge after crossing the ISR and entering the Iceland basin from the Nordic Seas. Two paths, through the Charlie–Gibbs Fracture Zone (CGFZ) and the Bight Fracture Zone (Lankhorst and Zenk, 2006; Zou and Lozier, 2016; Xu et al., 2018), connect the Iceland and Irminger basins passing the Mid–Atlantic Ridge. More recent model–based studies reveal an additional westward branch from the Iceland basin through the Reykjanes Ridge and crossing through the interior Irminger Sea towards the Labrador Sea (Xu et al., 2010; Zou et al., 2020a). The mean mid–depth circulation shows a confined current band west of the Reykjanes Ridge towards DS. South of DS it encounters the DSOW (Pickart, 1992; Dickson and Brown, 1994) and is transported further south around Greenland and the Labrador basin through the DWBC. A confined boundary current is established along the east Greenland shelf break. Once the western boundary current (WBC) passes Cape Farewell, while being partly dispersed, the WBC refocuses along the west Greenland shelf break. At Cape Desolation, where eddies are shed towards the interior Labrador Sea (Hátún et al., 2007; Prater, 2002; Lilly et al., 2003; Rieck et al., 2018) the WBC is partly dispersed and just north of it a bifurcation of the boundary current, following the $1,500$ and $3,000\ m$ isobaths of the northwestern Labrador Sea takes place (Cuny et al., 2002; Higginson et al., 2011; Palter et al., 2016; Fischer et al., 2018). At the coast of Labrador, the flow becomes confined in the boundary current again.

The importance of Labrador Sea convection for the strength and the variability of the AMOC is not finally understood and currently under debate (Lozier, 2012; Rhein et al., 2013). While some studies assume a direct linkage (Marshall and Schott, 1999; Yashayaev et al., 2008; Haine et al., 2008), others corroborate the assumption that the AMOC is only minimally impacted by Labrador Sea convection (Pickart and Spall, 2007; Zou and Lozier, 2016; Lozier et al., 2019; Petit et al., 2020). Deep convective mixing has been widely observed since the 1950s (Dietrich, 1957; Lazier, 1973) in the Labrador Sea and there are increasing observations of deep convection south of Cape Farewell and in the Irminger Sea (see Rühs et al. (2021)

for extensive literature collection). The interest in understanding exactly where the transformation from upper AMOC water to
lower AMOC water takes place in the SPNA has increased in recent years. Several studies within medium to high–resolution
ocean models have shown, that additionally to the deep convective mixing, diapycnal mixing between the basin interior and
the boundary currents as well as densification along the spreading pathways at the boundary currents play a crucial role for the
total formation of dense deep water. The question of the relative importance of these sources and their respective pathways for
the total deep water export towards the south and its variability is not completely clear yet (e.g. Straneo, 2006; Katsman et al.,
2018; Desbruyères et al., 2019; Sayol et al., 2019; Georgiou et al., 2020; Petit et al., 2020; Georgiou et al., 2021).

Newer research has shown that the very localized deep convection might only be adding transformed water to a major volume
of water transformed along the North Atlantic Current path (Desbruyères et al., 2019) and that the different transformation
processes seem to be related to different export time scales (Le Bras et al., 2020). Additionally, the observed deep convection
in the Irminger Sea increased over the past years (Våge et al., 2009; de Jong et al., 2012; Jong and Steur, 2016; Piron et al.,
2016; Fröb et al., 2016; de Jong et al., 2018). In contrast to the well documented southward spreading of deep water south of
$45°N$ from the subpolar gyre, the dynamics of formation and subsequent spreading of NADW within the SPNA are not so well
documented nor understood. In this model–based study, we present i) the relative contributions of the respective deep water
sources to the NADW transport at $53°N$ and ii) the pathways and advection time scales of the connections between $53°N$ and
the respective deep water sources. The methods and model used to perform the desired analyses are presented in the following
section 2. Subsequently, we present the sources and pathways of the single deep water sources in section 3.1. In section 3.2
the water mass properties of the different water masses are presented. To conclude and classify the results within the current
literature, the results are then controversially discussed in section 4.

2 Data and Methods

2.1 Lagrangian Experiments in VIKING20X-JRA-OMIP

The model output used to conduct our Lagrangian experiments is the eddy–rich nested ocean/sea–ice model configuration
VIKING20X-JRA-OMIP, as the name reveals forced by the JRA55–do forcing from 1958 to 2019 (version 1.4, Tsujino et al.,
2018, see Biastoch et al. (2021) for full model description). It is based on the global $1/4°$ resolution grid of the Nucleus for
European Modelling of the Ocean code (NEMO, version 3.6, Madec et al., 2017) and the Louvain la Neuve Ice Model (LIM2,
Fichefet and Maqueda, 1997). The tripolar $1/4°$ global horizontal grid is refined in the Atlantic Ocean to $1/20°$, yielding
an effective grid spacing of $\leq 5\,km$ in the SPNA. It contains 46 geopotential z–levels, increasing in thickness from $\sim 6\,m$
at the surface to $\sim 250\,m$ in the deepest layers. The daily three-dimensional Eulerian flow and hydrographic fields are used
here for the offline Lagrangian particle tracking experiments. Biastoch et al. (2021) show that the model is reproducing the
major dynamic properties in the region, such as the strength and width of the boundary currents as well as an AMOC strength
comparable to observations. To conduct the offline Lagrangian particle experiments, the Python module Parcels (version 2.2.2,
Delandmeter and Sebille, 2019) is utilised. Trajectories are estimated by advecting virtual particles along streamlines that are
calculated from the Eulerian flow field.
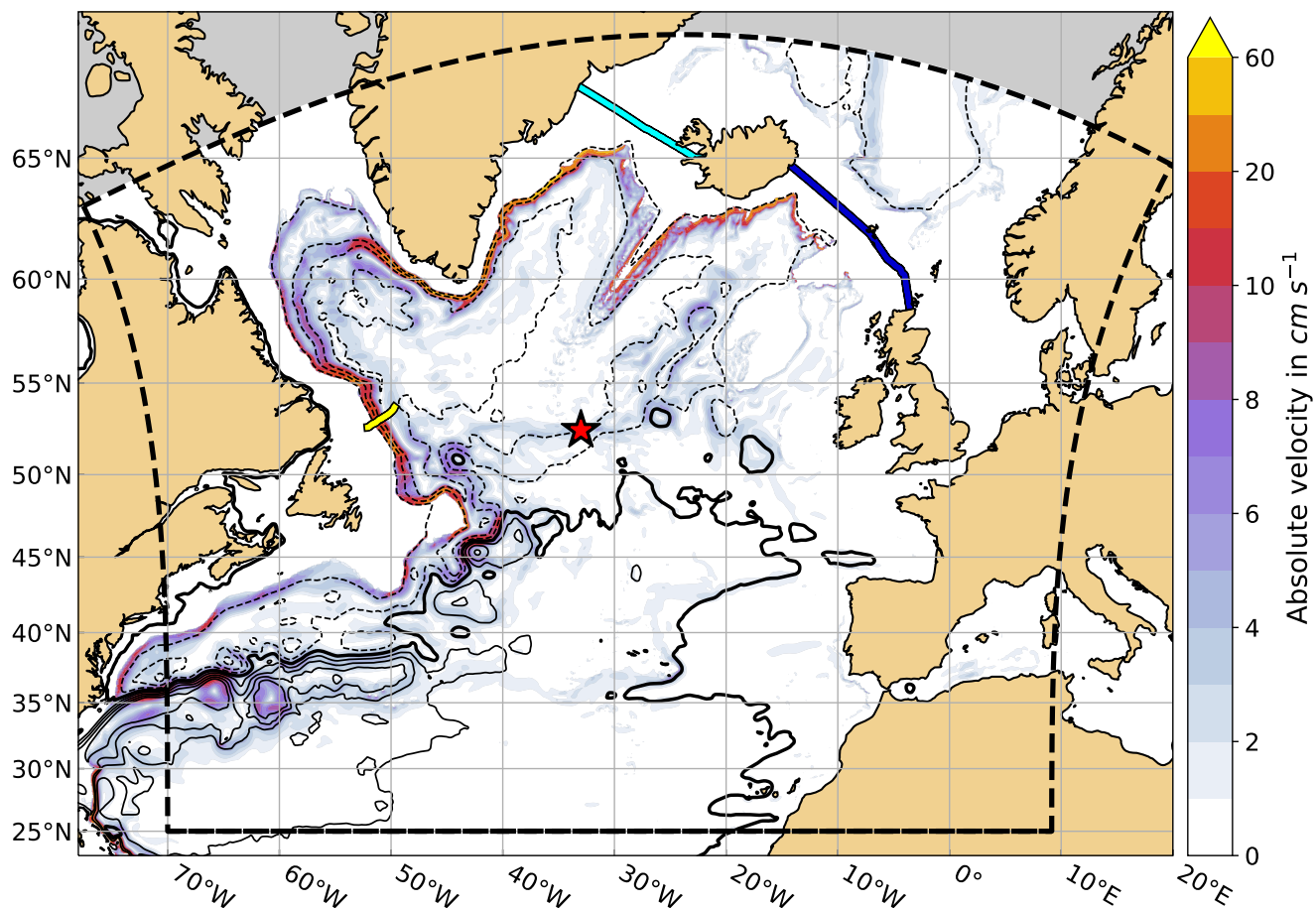
Figure 1. Mean absolute velocity (1958-2019, in $cm\ s^{-1}$, shading) at 1,298 m in VIKING20X-JRA-OMIP. The black contours are the mean barotropic stream function in 10 Sv intervals, where the thick black solid line marks 0 Sv. The Charlie–Gibbs Fracture Zone is indicated by the red star. The yellow line marks the $53°N$ section, the light and dark blue lines mark the Denmark Strait and Iceland–Scotland Ridge sections, respectively. The black dashed line indicates the boundary of the experiment domain considered in this study.

The domain, in which the Lagrangian particle experiments are conducted, is bounded to the north by the northern boundary of the high–resolution nest of VIKING20X (the northernmost point is $69.3°N$) and by $25°N$ to the south. The easternmost point is $20°E$, while the westernmost point is $77.5°W$. However, due to the tripolar grid of the model, the exact northern, eastern and western boundaries of the domain vary (see black dashed line in Figure 1).

Virtual particles are released along a section along the observational mooring array $53°N$ (Zantopp et al., 2017) off the coast of Newfoundland (yellow line in Figure 1), which is part of the Overturning in the subpolar North Atlantic Program (OSNAP, Lozier et al., 2017, 2019). The section in the model is approximated following the tripolar model grid in x- and y-direction (Handmann, 2019, chapter 4.3). Virtual particles are released daily during the period 2010 through 2019 in each grid box along

100 this section. Following Schmidt et al. (2021), the amount of particles released in each grid box is defined relative to the volume transport associated with each individual grid box. If V_{gb} is the volume transport of a given grid box and $V_{th} > 0$ a volume transport threshold, determining the maximum absolute volume transport assigned to an individual particle, then the number of particles N_{gb} released within the given grid box is defined by:

$$N_{gb} = ceil \left(\frac{|V_{gb}|}{V_{th}} \right) \tag{1}$$

105 The volume transport V_{P_i} assigned to each particle P_i within a grid box is then defined as:

$$V_{P_i} = \frac{|V_{gb}|}{N_{gb}} \tag{2}$$

where $i = 1...N_{gb}$. Subsequently, particles are only released in grid boxes where $|V_{gb}| > 0$. For grid boxes where $0 < |V_{gb}| \leq V_{th}$ only one particle is released, which is assigned exactly the absolute transport that is associated with the corresponding grid box. If $|V_{gb}| > V_{th}$, the transport associated with the given grid box is distributed equally among multiple particles P_i. Thus,

110 each particle is associated with a pre–defined volume transport value $V_{P_i} \leq V_{th}$ that varies among particles from different grid boxes.

The release positions of the individual particles are determined by randomly distributing the particles across their corresponding grid box. In the present case, particles are only released in south–eastward directed flow. The maximum volume transport allowed per particle is $0.1\ Sv$. This results in a total of approximately 8.9×10^6 particles being released.

115 The virtual particles are integrated backwards in time for $14,600$ days, or ~ 40 years using a 4th order Runge–Kutta scheme at a time step of 5 minutes. Since no additional diffusion kernel is applied, the obtained particle trajectories are equivalent to volume transport pathways (Schmidt et al., 2021). An additional kernel is however incorporated to sample temperature, salinity and mixed layer depth along the particles' trajectories. Note that Parcels assumes tracer values to be constant within individual grid boxes for Arakawa C-type grids (Delandmeter and Sebille, 2019). The particle positions and properties are stored at daily

120 resolution.

2.2 Categorisation of Particles

Here we focus on NADW, hence, only particles released within this water mass are considered during the analyses. The water mass boundaries are defined as mean density values over the complete model output, covering 1958 through 2019. The upper boundary of NADW is the density of the AMOC maximum at OSNAP, in VIKING20X-JRA-OMIP defined as $\sigma_{DW} = \sigma_0 = $

125 $27.62\ kg\ m^{-3}$ (Biastoch et al., 2021). The LSW is defined as $27.62\ kg\ m^{-3} \leq \sigma_0 < 27.86\ kg\ m^{-3}$. Consequently, the lNADW in the model is found at $\sigma_0 \geq 27.86\ kg\ m^{-3}$ (Handmann et al., 2018; Biastoch et al., 2021).

Accordingly, the particle experiments are subsampled to the subset of particles released with densities $\sigma_0 \geq \sigma_{DW}$ and are referred to as $NADW_P$, amounting to approximately 3.5×10^6 particles. Once the particles belonging to the NADW water mass are identified, these particles are divided into five mutually exclusive categories. The categories are defined based on the

130 particles' sources. For each particle the trajectory is considered only between the particle's source, as defined in the following,

and $53°N$. In consequence, trajectories are truncated and do not encompass the same advection time. However, all resulting trajectories lie entirely within the NADW density range and within the North Atlantic.

Note that despite being calculated backwards in time, the trajectories are referred to in their forward sense in the following, i.e. in flow direction. Consequently, the particle release at $53°N$ constitutes the last time step or end of the trajectory.

135 Particles that cross the Greenland–Scotland Ridge (GSR) and retain densities of $\sigma_0 \geq \sigma_{DW}$ represent NADW crossing the GSR from the Nordic Seas into the SPNA. The section which particles need to cross in order to be taken into account here is a combination of two subsections, the DS and the ISR. The particles are classified as DS_P or ISR_P depending on the section they cross. The subsections are extracted from the model grid as described in Handmann (2019, chapter 4.3). In Figure 1 the two sections are indicated by the blue lines. Particle information along the respective trajectories is only considered between the

140 last crossing of the GSR and arriving at $53°N$. Therefore, parts of the trajectories lying within the Nordic Seas or recirculating over the GSR are not considered.

If particles increase their density during the experiment from $\sigma_0 < \sigma_{DW}$ to $\sigma_0 \geq \sigma_{DW}$ before reaching $53°N$ outside of the mixed layer, this is referred to as diapycnal mass flux and the particles are classified as DIA_P. Else, if the respective density increase occurs within the mixed layer, the particles are classified as ML_P. The pivotal density change of a particle is the last

145 increase from $\sigma_0 < \sigma_{DW}$ to $\sigma_0 \geq \sigma_{DW}$ before reaching $53°N$, hence the exact processes and property changes in the mixed layer are not explicitly considered here. For DIA_P trajectories are only considered between the respective density increase and reaching $53°N$. For ML_P trajectories are considered between leaving the mixed layer and arriving at $53°N$.

The particles that can not be assigned to any of the previous categories form the last category. Particles belonging to this category retain densities $\sigma_0 \geq \sigma_{DW}$ throughout their entire advection time and are referred to as RES_P. These particles either

150 reside within the North Atlantic during the whole experiment, or enter the domain at any point in time through its lateral boundaries, except through the GSR.

It is important to point out that every particle belonging to any of the described categories can still be entrained into the mixed layer. These mixed layer contacts are then, however, not associated with a densification from $\sigma_0 < \sigma_{DW}$ to $\sigma_0 \geq \sigma_{DW}$.

In order to differentiate the region of densification the particle categories are further divided by their position above topogra-

155 phy. If the underlying bathymetry is shallower than $3{,}000\,m$ the particle is classified as being in the boundary, if the bathymetry is deeper, the density transition is located in the basin interior.

2.3 Analyses

In the following, all volume transport estimates are given with respect to the 10-year mean NADW volume transport at $53°N$ of $30.1\,Sv$ from 2010 to 2019. First, particles are grouped based on a certain condition (e.g. region of origin). Then the cumulative

160 transport of all particles within a group is divided by the cumulative transport of all $NADW_P$. The obtained fraction is then multiplied by the mean transport at $53°N$ to obtain the mean volume transport associated with the defined particle group.

To derive the relative and absolute *transport contributions* of the different volume transport sources, the particles are separated into the five categories, as described in section 2.2. The corresponding contributions are then estimated as explained above.

165   In order to compute the *transport distribution* at $53°N$ particles are grouped into $5\,km \times 0.01\,kg\,m^{-3}$ bins, where the distance refers to the horizontal distance from the starting point of the section. To obtain a depth profile, the transport is then summed over all distance bins and two density bins each, resulting in $0.02\,kg\,m^{-3}$ bins.

To evaluate the *horizontal pathways* of the particles, we follow section 4.3 in van Sebille et al. (2017). The pathways in the horizontal plane that are associated with most of the volume transport conducted by the particles, are calculated as

170   transport–weighted probability maps. In order to do so, a regular longitude–latitude grid is defined, in this case $0.25° \times 0.25°$. As described above, the cumulative transport of particles crossing a particular grid cell is estimated. Each particle is only accounted for once per grid cell. The cumulative transport per grid cell is then divided by the cumulative transport of all particles released within the NADW's σ_0 range. Therefore, the transport–weighted fraction of particles visiting a certain grid cell at least once is obtained. Within each grid cell values can range between 0 and 1, or 0 and 100%, equivalently. This would

175   be the case if none (0%) or all (100%) particles pass through the same grid cell. In the following, grid cells with values $< 0.01\%$ are masked out.

The point where a particle changes its density from $\sigma_0 < \sigma_{DW}$ to $\sigma_0 \geq \sigma_{DW}$ is referred to as the particle's origin in the following. This *point of origin* of each particle trajectory is determined as described in section 2.2. The particles are then binned into $0.5° \times 0.5°$ longitude–latitude bins, based on their respective starting points. Grid cells with values $< 10^{-4}\,Sv$ are

180   masked out. To determine the transport contributions of the Labrador and Irminger Seas, the transport is integrated over all grid cells within the respective basin. The Labrador Sea basin is bounded by $43.5°W$ to the east and $52°N$ to the south, while the Irminger Sea basin is bounded by $43.5°W$ to the west, $25°W$ to the east and $52°N$ to the south. The Iceland basin is bounded by $25°W$ to the west and $52°N$ to the south. To the north–east this area is bounded by the ISR (see blue dashed lines in Figure 2). The remaining area south of $52°N$ is referred to as southern SPNA in the following.

185   For each particle the time it takes from its respective point of origin to reach $53°N$ is calculated. Then the particles are grouped based on their *travel times* into 1 month bins. The transport per bin is estimated as described above. Additionally, the transport is summed over all bins, cumulatively.

Particles are also grouped by their water mass properties at their respective source, as well as at $53°N$. The considered properties are σ_0, absolute salinity (S_A) and conservative temperature (Θ), with bin sizes of $0.025\,kg\,m^{-3}$, $0.01\,g\,kg^{-1}$ and

190    $0.2°C$, respectively. These properties were computed from the practical salinity, potential temperature and depth tracked along each trajectory using the TEOS-10 toolbox for Python (Intergovernmental Oceanographic Commission, 2015). To obtain the *volumetric water mass transformations*, the difference between $53°N$ and the particle source is calculated for each σ_0, S_A and Θ class.

To evaluate the *evolution of the particle properties* along the individual pathways, the maximum or minimum salinity or

195   temperature is determined along a particle trajectory. Then the location along the trajectory is determined where the difference in salinity or temperature between the extreme and the particle source is halved. Based on these locations the particles are then grouped into $0.5° \times 0.5°$ longitude–latitude bins and the transport–weighted mean particle depth per bin is estimated.
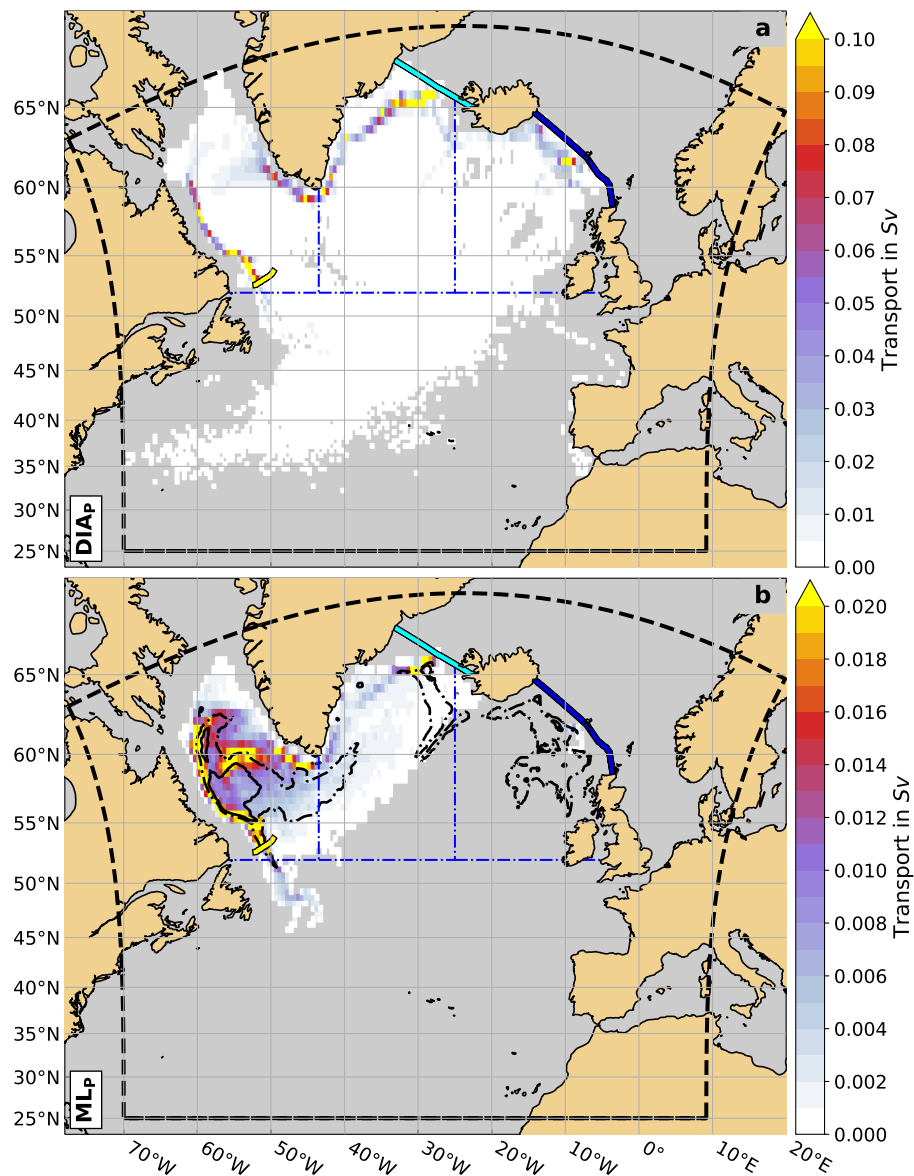
Figure 2. Locations of origin, calculated as mean transport in Sv (shading, $1/2° \times 1/2°$ bins) for (a) DIA$_P$ and (b) ML$_P$ (see section 2.2 for details of the definitions). In (b), the black solid contour marks the 2000-2019 mean DJFM mixed layer depth of $500\,m$. The black dash–dotted contour marks the 2000-2019 mean of the annual maximum mixed layer depth of $500\,m$. The yellow line marks the $53°N$ section, the light and dark blue lines mark the Denmark Strait and Iceland–Scotland Ridge sections, respectively. The black dashed line indicates the boundary of the experiment domain. The blue dash–dotted lines indicate the areas which are used to calculate the Labrador Sea, the Irminger Sea and the Iceland basin volume transport contributions.

Table 1. Mean transport from 2010-2019 in Sv at $53°N$ associated with each particle category (DIA$_P$, ML$_P$, DS$_P$, ISR$_P$ and RES$_P$), as detailed in section 2.2, as well as their relative contributions in % for $\sigma_0 \geq 27.62\ kg\ m^{-3}$ (NADW), $27.62 \leq \sigma_0 < 27.86\ kg\ m^{-3}$ (LSW) and $\sigma_0 \geq 27.86\ kg\ m^{-3}$ (lNADW).

	NADW	LSW	lNADW
total transport	$30.1\ Sv$	$26.7\ Sv$	$3.4\ Sv$
	100%	100%.	100%
DIA$_P$	$14.3\ Sv$	$12.8\ Sv$	$1.5\ Sv$
	48%	48%	44%
ML$_P$	$7.2\ Sv$	$7.0\ Sv$	$0.2\ Sv$
	24%	26%	5%
DS$_P$	$3.8\ Sv$	$3.4\ Sv)$	$0.4\ Sv$
	13%	13%	11%
ISR$_P$	$1.9\ Sv$	$1.7\ Sv$	$0.2\ Sv$
	6%	6%	5%
RES$_P$	$2.9\ Sv$	$1.7\ Sv$	$1.2\ Sv$
	10%	7%	34%

3 Results

3.1 Sources, Pathways and Advection Time Scales

200 The mean southward NADW transport in the presented Lagrangian experiments shows two peaks in density space, the first of which is located within the LSW component around $\sigma_0 = 27.80\ kg\ m^{-3}$. A secondary peak is found just within the lNADW density range around $\sigma_0 = 27.87\ kg\ m^{-3}$ (Figure 3 i). The upper transport peak is associated with transport peaks around $27.80\ kg\ m^{-3}$ for all four defined particle sources (Figure 3 iii-vi). The dense maximum (Figure 3 i) on the other hand is dominated by diapycnal mass flux and the particle residuum (Figure 3 ii-iii). Diapycnal mass flux dominates the transport 205 distribution throughout the water column with an overall mean transport of $14.3\ Sv$ (48%) (Table 1 and Figure 3). For the LSW component above $27.86\ kg\ m^{-3}$ DIA$_P$ amount to $12.8\ Sv$ (48%), with the second largest contributor being particles from the mixed layer ($7.0\ Sv$ or 26%) (Table 1). The lNADW component (below the red dashed line in Figure 3) is dominated by DIA$_P$ with $1.5\ Sv$ (44%), while the second largest contribution, $1.2\ Sv$ (34%), is associated with RES$_P$ (Table 1). Overall DS$_P$ contribute $3.8\ Sv$ (13%) to the southward NADW transport at $53°N$, with about $3.4\ Sv$ (13%) within the LSW component 210 and $0.4\ Sv$ (11%) in the lNADW component. ISR$_P$ amount to $1.9\ Sv$ (6%) throughout the NADW σ_0 range, with $1.7\ Sv$ (6%) within the LSW density range and $0.2\ Sv$ (5%) within the lNADW density range (Table 1).

The main spreading pathways from the respective sources to $53°N$ are largely concentrated within the boundary currents for all four particle categories (Figure 4). In the north–eastern Labrador Sea, near Cape Desolation (west of Greenland), the pathways fan out for all categories, most probably related to the eddy activity here, namely the shedding of Irminger rings.
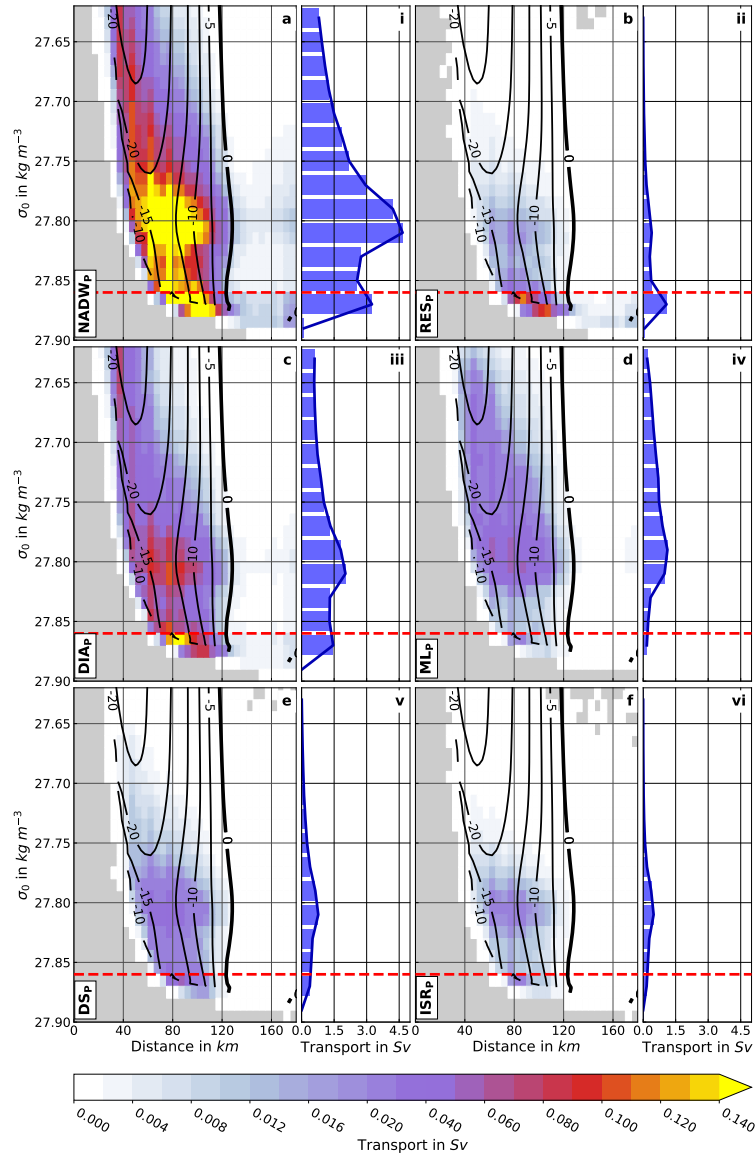
Figure 3. Mean transport distribution at $53°N$ in Sv in density space (a to f, shading, $5\ km \times 0.01\ kg\ m^{-3}$ distance–density bins) and mean transport accumulated along $53°N$ in Sv (i to vi), $0.02\ kg\ m^{-3}$ bins). The red dashed lines mark the mean $\sigma_0 = 27.86\ kg\ m^{-3}$ isopycnal (upper boundary of lNADW in the model). Black contours in a to f are mean meridional velocities in $cm\ s^{-1}$. Note the non–linear colour scale ($0.002\ Sv$ intervals up to $0.02\ Sv$ and $0.01\ Sv$ intervals starting from $0.02\ Sv$) for a to f. Mean transport distributions are shown for (a/i) NADW$_P$, (b/ii) RES$_P$, (c/iii) DIA$_P$, (d/iv) ML$_P$, e/v DS$_P$ and (f/vi) ISR$_P$ (see section 2.2 for details of the definitions).

215   Furthermore, all particle categories exhibit pathways extending southward from $53°N$ (Figures 4). These pathways become more distinct on longer time scales and represent the recirculation south of $53°N$ at the Orphan Knoll region (not shown).
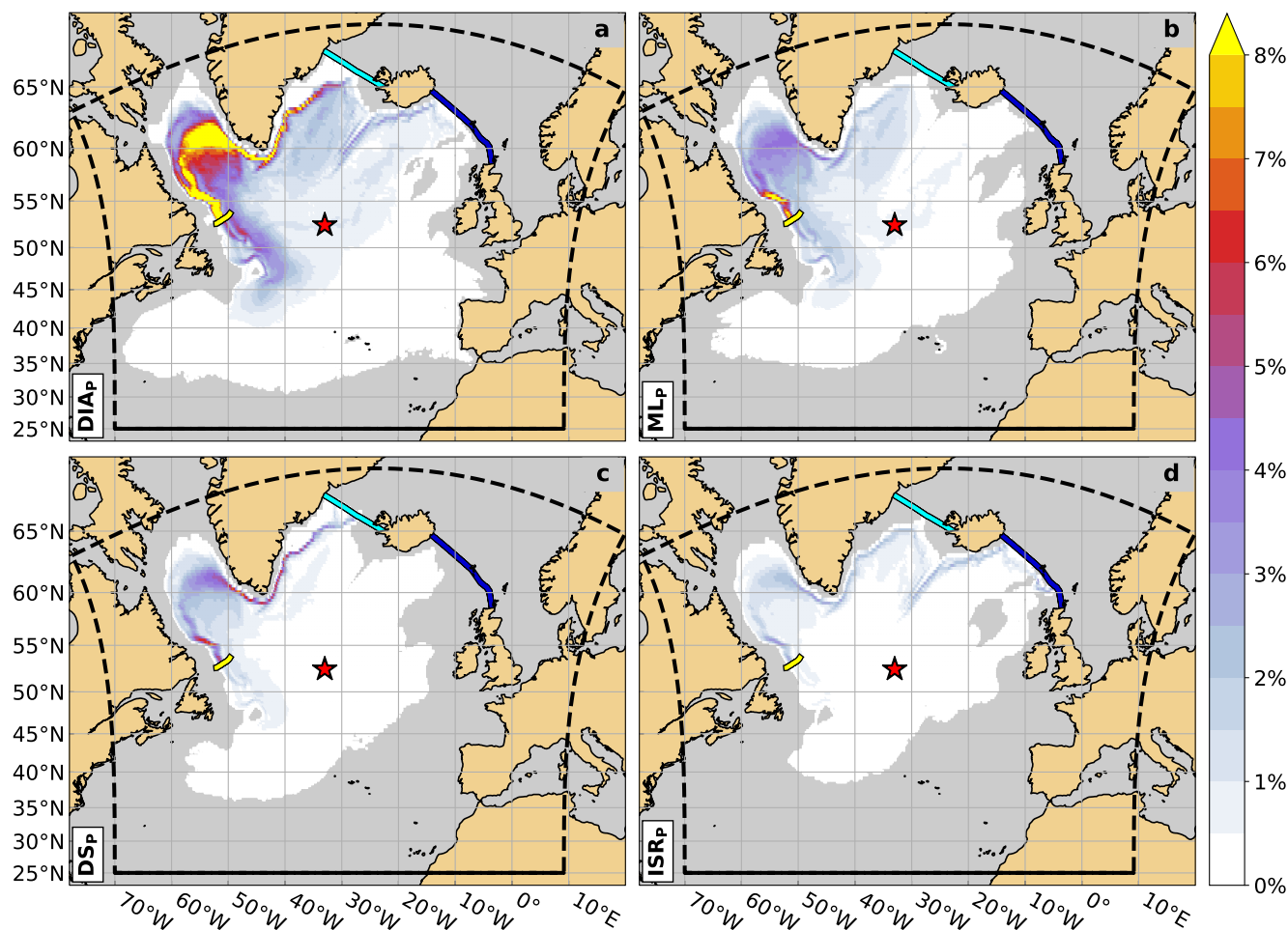
Figure 4. Particle pathways associated with most of the volume transport, calculated as transport–weighted probability density maps ($1/4° \times 1/4°$ bins) of the different particle categories: (a) DIA_P, (b) ML_P, (c) DS_P and (d) ISR_P (see section 2.2 for details of the definitions). The Charlie–Gibbs Fracture Zone is indicated by the red star. The yellow line marks the $53°N$ section, the light and dark blue lines mark the Denmark Strait and Iceland–Scotland Ridge sections, respectively. The black dashed line indicates the boundary of the experiment domain.

3.1.1 Diapycnal Mass Flux

About half the NADW transport at $53°N$, $14.3\,Sv$ (48%), is associated with diapycnal mass flux (Table 1). The majority of DIA_P enter the NADW density range within the boundary current in the Labrador Sea ($5.5\,Sv$) and Irminger Sea ($4.6\,Sv$) in depths between 600 and $1,100\,m$ (not shown). Only a very small portion is added in the basin interiors (Figure 2 a, Table 2) at depths below $1,300\,m$ (not shown). The Iceland basin, adding $2.4\,Sv$, and the southern SPNA, adding $1.1\,Sv$, consequently play only a small role for the total NADW with DIA_P origin. After their densification, particles of this category spread, additionally to the boundary currents, throughout the basin interior of the western SPNA with further pathways from the
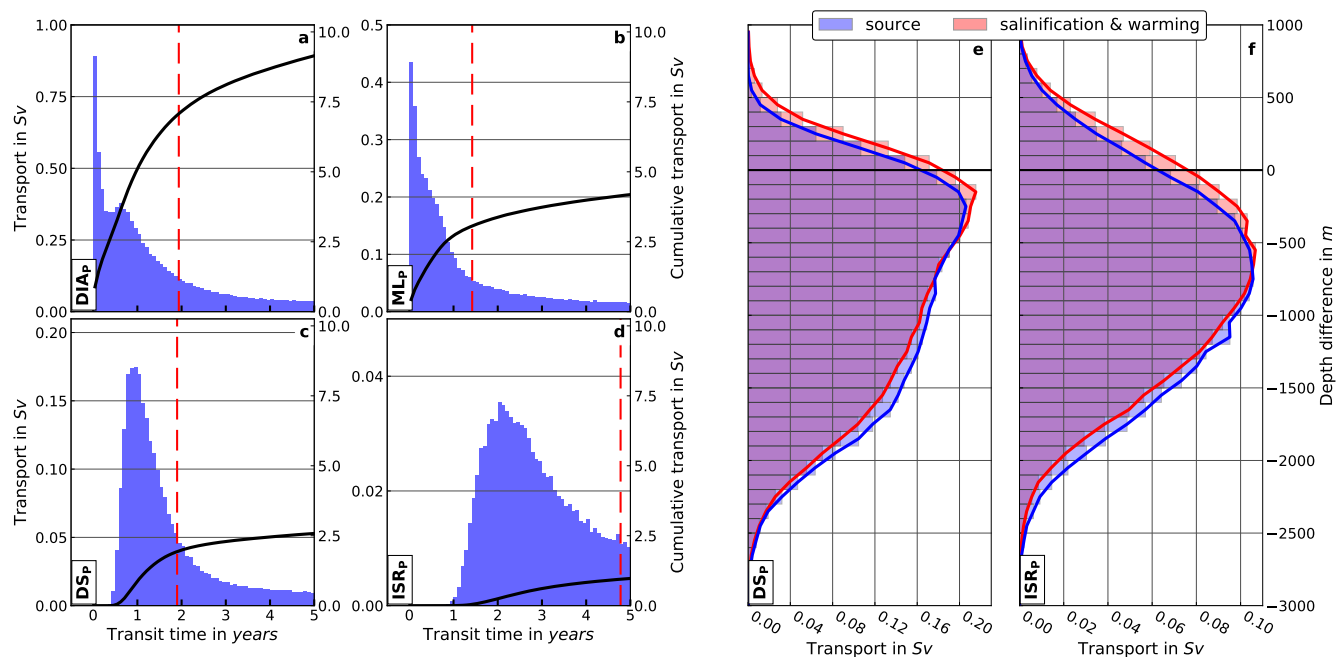
Figure 5. (a-d) Transit time distributions, calculated as mean volume transport in Sv (bars, lefthand scale) and cumulative mean volume transport in Sv (black lines, righthand scale) as a function of transit time (1 $month$ bins) for (a) DIA_P, (b) ML_P, (c) DS_P and (d) ISR_P (see section 2.2 for details of the definitions). The red dashed lines mark the time after which half the transport associated with the respective category has reached $53°N$. Note the different y-axis scales for the bar plots.

(e-f) Evolution of particle depth between the particle source (blue) and $53°N$, as well as between the location where the major salinity and temperature increase occurs (red) and $53°N$, calculated as the mean transport per depth difference bin ($100\,m$) in Sv for (e) DS_P and (f) ISR_P.

Table 2. Mean transport contributions (2010-2019) from the Labrador Sea (LS) and Irminger Sea (IS), the Iceland basin, as well as the remaining SPNA south of $52°N$ (southern SPNA) in Sv. The regions are outlined by the blue dash–dotted lines in Figure 2. The Labrador and Irminger Sea contributions are separated into an interior and boundary component (water depths shallower than $3,000\,m$). Transport contributions are given for DIA_P and ML_P (see section 2.2 for details of the definitions).

		LS		IS		Iceland	southern
		interior	boundary	interior	boundary	basin	SPNA
DIA_P	NADW	$0.6\,Sv$	$5.5\,Sv$	$0.1\,Sv$	$4.6\,Sv$	$2.4\,Sv$	$1.1\,Sv$
	LSW	$0.6\,Sv$	$5.0\,Sv$	$0.1\,Sv$	$4.1\,Sv$	$2.2\,Sv$	$0.8\,Sv$
ML_P	NADW	$2.6\,Sv$	$3.3\,Sv$	$0.2\,Sv$	$0.8\,Sv$	$< 0.1\,Sv$	$0.2\,Sv$
	LSW	$2.5\,Sv$	$3.3\,Sv$	$0.2\,Sv$	$0.8\,Sv$	$< 0.1\,Sv$	$0.2\,Sv$

Iceland basin following the $1,000\,m$ isobath along the Reykjanes Ridge and through the CGFZ. Most particles pass through
the central Labrador Sea before exiting it via the DWBC at $53°N$ (Figure 4 a). Most of the DIA_P are formed within the LSW
density class, where the Labrador Sea exceeds the Irminger Sea by $1.4\,Sv$. Similar amounts of lNADW ($\sim 0.5\,Sv$) are added
in both basins, with the Iceland basin and the southern SPNA again only playing a minor role with 0.2 and $0.3\,Sv$, respectively
(Table 2). The respective maxima of the mean transport are found just south of DS until $65°N$, east and west of Cape Farewell
and between Hamilton Bank and $53°N$. Minor contributing regions are found along the continental slopes south of the ISR,
the Reykjanes Ridge and within the Labrador Sea most probably following the eddy track of Irminger Rings shed at Cape
Desolation (Prater, 2002; Hátún et al., 2007; Rieck et al., 2018). Contrary to the boundary current, single regions in the interior
do not show as elevated values though they are spread over a larger area (Figure 4 a). These patterns of the total NADW are
similarly found for the LSW and lNADW (not shown). As the particle sources are located within or nearby boundary currents,
which exhibit strong velocities, the particles can have rather short transit times. The transit time distribution peaks between 0
and 1 years, with more than a third of the volume transport associated with DIA_P reaching $53°N$ within this time span. After
approximately 1.94 years 50% of the transport associated with DIA_P has passed $53°N$ (Figure 5 a).

3.1.2 Mixed Layer

The second largest supplier of NADW, with $7.2\,Sv$ (24%) of the $30.1\,Sv$ of NADW passing $53°N$, was found to originate from
the mixed layer (ML_P, Table 1). The particles leave the mixed layer between November and June with a peak export between
February and April (not shown) dominantly within the central Labrador Sea or the Boundary Current along the Labrador
shelf break (Figure 2 b). Elevated values can also be found south of DS and west of the Faroe Islands, which could possibly
be related to the shallow pathways of the particles at these locations. There are minor, but noticeable contributions from the
Irminger Sea and south–west of Cape Farewell. These particles tend to leave the mixed layer at shallower depths and lower
densities compared to particles from the Labrador Sea (Figure A1). The Labrador Sea, however, dominates as source region of
this particle category with $5.9\,Sv$ (82% of the total ML_P transport) compared to $1.0\,Sv$ (14% of the total ML_P transport) from
the Irminger Sea (Table 2). Within the Labrador Sea, the contribution from the boundary regions dominates with $3.3\,Sv$ over
the interior contribution with $2.6\,Sv$ (Table 2). Half the volume transport associated with ML_P reaches $53°N$ within 1.42 years
which we expected due to the close proximity of the source regions to $53°N$.

3.1.3 GSR

With $5.7\,Sv$ (19%) of the NADW transport at $53°N$, the water passing DS (DS_P, $3.8\,Sv$ or 13%) and the ISR (ISR_P, $1.9\,Sv$ or
6%) are the third biggest source of supply for NADW passing $53°N$ (Table 1). These volume transports are comparable with
previous model analysis (DS: $3.1 \pm 0.4\,Sv$ and ISR $1.3 \pm 0.2\,Sv$; Biastoch et al. (2021)). These values compare well with the
Transport estimates from observations, ranging from $3.1\,Sv$ (Jochumsen et al., 2017) to $3.5\,Sv$ (Harden et al., 2016) at DS and
are slightly lower than the observed $2.2\,Sv$ (Hansen et al., 2016; Rossby et al., 2018) to $2.7\,Sv$ (Berx et al., 2013) at the ISR.

Particles that pass through *DS* within the NADW density range populate majorly the two $\sim 600\,m$ deep troughs of the strait,
with domination of the deeper one just west of Iceland (Figure 4 c). Both pathways then merge south of DS and follow the East

and West Greenland shelf break until reaching the Labrador Sea. DS$_P$ have a density between 27.70 and 27.88 $kg\ m^{-3}$ (Figure 3 e, v). The longer the particles take to reach $53°N$, the more particles recirculate through the basin interiors of the Irminger and the Labrador Sea (not shown). The transit time distribution peaks between 1 and 2 years of advection (Figure 5 c), with 260 50% of the associated transport arriving at $53°N$ within 1.90 years.

NADW particles crossing the *ISR* are strongly concentrated within the boundary currents after entering the SPNA majorly through the Faroe Bank channel and a trough in the Iceland–Faroe Ridge just east of Iceland (Hvalbakshalli slope, Hjartarson et al., 2017, Figure 4 d). ISR$_P$ surround the Reykjanes Ridge between the $1,000$ - $2,000\ m$ isobaths and do not majorly pass through the CGFZ. The longer the particles take to reach $53°N$, the more particles tend to be advected through the basin 265   interior of the SPNA (not shown). Due to the longer pathways of these particles, transit times tend to be longer. The transit time distribution peaks between 2 and 3 years (Figure 5 a-c), with 50% of the associated transport arriving at $53°N$ within 4.78 years. The decay with increasing transit times relative to the peak value is slowest for this category, due to the importance of interior pathways.

Assuming that the shortest transit times are associated with the shortest distances travelled by the particles within a specific 270   particle category, the average velocity a particle must at least have to reach $53°N$ can be calculated. This velocity is estimated to be $\sim 19\ cm\ s^{-1}$ for ISR$_P$ and $\sim 25\ cm\ s^{-1}$ for DS$_P$. Similar values are found for particles from the mixed layer and associated with diapycnal mass flux originating from areas close to the GSR. These values seem reasonable given the fact that mean velocities can easily exceed $20\ cm\ s^{-1}$ and reach more than $50\ cm\ s^{-1}$ at various depth levels in VIKING20X (e.g Figure 7 in Biastoch et al. (2021)).

275   **3.1.4   Residuum**

The volume that is not attributable to any of the above defined sources of NADW after 40 years of advection amounts to $2.9\ Sv$ (10%, Table 1). This residuum (RES$_P$) can be separated into particles circulating within the experiment domain for 40 years and particles entering the domain across the southern boundary ($25°N$) or through Davis Strait. Particles circulating for 40 years within the domain contribute $2.1\ Sv$ (72% of the total RES$_P$ transport). Particles entering from the south contribute 280 $0.8\ Sv$ (28% of the total RES$_P$ transport) and particles passing through Davis Strait contribute $< 0.1\ Sv$ ($< 2\%$ of the total RES$_P$ transport) (not shown). The majority of RES$_P$ recirculate in the basin interior of the SPNA (not shown). The pathways of the denser particles are mostly situated west of the Mid–Atlantic Ridge, while particles with lower densities are advected throughout the whole SPNA this emerges once the analysis is done in σ_2 (not shown). Most particles that cross the Mid–Atlantic Ridge pass through the CGFZ.

285   **3.2   Water Mass Transformations**

Ordered by the relative contribution to the transport at $53°N$ we evaluate the changes water parcels undergo during their spreading routes from their point of origin to the $53°N$ target section. All particle categories, apart from RES$_P$, show similar water mass property signatures at $53°N$. Hence, depending on the properties of absolute salinity (S_A), conservative temperature (Θ) and density (σ_0) at the point of origin the water parcels undergo dissimilar changes along their pathways. Particles of DIA$_P$

Table 3. Mean water mass property modifications of the four particle categories DIA$_P$, ML$_P$, DS$_P$ and ISR$_P$ (see section 2.2 for details of the definitions). Listed are potential density (referenced to 0 $dbar$, σ_0), absolute salinity (S_A), conservative temperature (Θ) and the transformed volume in Sv from source to $53°N$ (target section). When values are presented with "/", two major classes of properties are persistent for this particle category.

	property	source	$53°N$	transformed volume
DIA$_P$	S_A	$35.2\ g\ kg^{-1}$	$35.16\ g\ kg^{-1}$	$8.0\ Sv$
$(14.3\ Sv)$	Θ	$5.4°C$	$3.8°C$	$9.3\ Sv$
	σ_0	$27.65\ kg\ m^{-3}$	$27.80\ kg\ m^{-3}/27.85\ kg\ m^{-3}$	$8.9\ Sv$
ML$_P$	S_A	$35.14\ g\ kg^{-1}$	$35.16\ g\ kg^{-1}$	$1.9\ Sv$
$(7.2\ Sv)$	Θ	$4.0°C$	$3.8°C$	$1.2\ Sv$
	σ_0	$\sim 27.75\ kg\ m^{-3}$	$27.78\ kg\ m^{-3}$	$1.7\ Sv$
DS$_P$	S_A	$35.09\ g\ kg^{-1}$	$35.16\ g\ kg^{-1}/35.19\ g\ kg^{-1}$	$2.6\ Sv$
$(3.8\ Sv)$	Θ	$0.8°C/2.8°C$	$3.7°C$	$3.1\ Sv$
	σ_0	$27.98\ g\ kg^{-1}/27.87\ kg\ m^{-3}$	$27.80\ kg\ m^{-3}/27.87\ kg\ m^{-3}$	$2.9\ Sv$
ISR$_P$	S_A	$35.08\ g\ kg^{-1}$	$35.16\ g\ kg^{-1}/35.19\ g\ kg^{-1}$	$1.4\ Sv$
$(1.9\ Sv)$	Θ	$0.2°C$	$3.7°C$	$1.6\ Sv$
	σ_0	$28.05\ kg\ m^{-3}$	$27.80\ kg\ m^{-3}$	$1.5\ Sv$

290 and ML$_P$ origin densify during spreading through cooling and freshening, whereas DS$_P$ and ISR$_P$ lighten from source to target through warming and salinification. Volume–wise, the water mass transformations are more pronounced for DIA$_P$ and DS$_P$ than for ML$_P$ and ISR$_P$ (Table 3).

3.2.1 DIA$_P$

The water parcels associated with diapycnal mass flux undergo a significant cooling of $\Delta\Theta = -1.6°C$, and freshening of
295 $\Delta S_A = -0.04\ g\ kg^{-1}$ along their pathways towards $53°N$. The freshening value arises from the salinity signature of DIA$_P$ at origin and target (Table 3 and Figure A2).

Freshening occurs mostly along the western flank of the Reykjanes Ridge, along the continental slope around Greenland and off Labrador, as well as in the interior Labrador Sea (Figure A3 a). East of Cape Farewell, the freshening occurs at depths around $1,300$ to $1,500\ m$. South of Cape Farewell and Cape Desolation values reach up to $\sim 2,000\ m$, while within the
300 Labrador Sea the freshening occurs mostly shallower than $1,000\ m$. Within the interior SPNA the transformation can occur at depths deeper than $2,000\ m$, however, these transformations are less important in terms of volume (Figure A3 a). Locations and depths of the cooling are similar to the freshening (Figures A3 b and A3 d), however, volume–wise the cooling is less pronounced along the eastern flank of the Reykjanes Ridge compared to the freshening (Figure A3 a-b).

The cooling dominates over the freshening leading to a density increase (from $\sigma_0 = 27.65\ kg\ m^{-3}$ to $\sigma_0 = 28.05\ kg\ m^{-3}$)
305 and narrows the property ranges of all three variables at $53°N$ compared to the source regions. Due to the nature of the

diapycnal mass flux the intensive change of particle properties along the spreading pathways between source and target region is not surprising. As described in section 3.1, most DIA$_P$ particles originate from the shelf breaks around Greenland and the Labrador Sea and get advected along the boundary current, where more property exchange with the ambient shelf water, leading to freshening, and exchange with the atmosphere can occur within the NADW property range.

310 ### 3.2.2 ML$_P$

At their source regions, particles from the mixed layer are cooler and fresher than DIA$_P$ at their respective origin (Table 3). In this experiment particles from the mixed layer majorly originate from the Labrador Sea with slight domination of the boundary regime ($3.3\ Sv$) over the basin interior ($2.6\ Sv$). A small volume also originates from the southeast of the section and reaches $53°N$ after recirculation at Orphan Knoll (Figure 2 b). Only a relatively small amount of particles originate

315 from the regions where the deepest mixed layers occur (black solid line in Figure 2 b). Due to the definition of the origin of ML$_P$, which is associated with the point where the particle exits the mixed layer within the NADW density, this is not surprising. The property transition occurs majorly in the marked mixed layer (Figure 2 b) and the water parcels are then advected to the associated export point (origin) outside of the marked area. Hence, the origin locations only partially coincide with regions where deep mixed layers potentially can occur (black dash–dotted line in Figure 2 b). ML$_P$ show a smaller value

320 range compared to DIA$_P$ for all three parameters (Figure A2). Even though no distinct peak is discernible in the ML$_P$ σ_0 signature at their origin ($\Theta = 4.0°C$, $S_A = 35.14\ g\ kg^{-1}$), a slight cooling and salinity increase is apparent, leading to a slight densification ($\Theta = 3.8°C$, $S_A = 35.16\ g\ kg^{-1}$ and $\sigma_0 = 27.78\ kg\ m^{-3}$ (Table 3 and Figure A2). These properties at origin and $53°N$ compare well with literature values for LSW (Liu and Tanhua, 2021). ML$_P$ undergo the least volumetric transformation of the presented particle categories. This is not surprising, as ML$_P$ are densified through convection and then, once cut off from

325 the atmosphere, advected majorly adiabatically.

3.2.3 GSR

In contrast to the particles of the DIA$_P$ and ML$_P$ categories, the particles originating from DS$_P$ and ISR$_P$ spread predominantly along the boundary currents. As mentioned before, DS$_P$ feature a mixture of different water types with similar salinity ($S_A = 35.09\ g\ kg^{-1}$) and varying temperature signature (close to Greenland shelf: $\Theta = 0.8°C$; close to Iceland: $\Theta = 2.8°C$) within

330 the NADW, but both undergo similar transitions south of DS (Table 3). DS$_P$ and ISR$_P$ both feature a decrease in density due to similar property transitions along their spreading pathways, as they undergo a substantial salinity increase and warming (Table 3 and Figure A5). For the decrease in density, the temperature increase dominates over the increase in salinity. The salinity increase (to the point where 50% of the total increase is reached) occurs for both particle categories just after crossing the GSR ridge; close to the East Greenland shelf break just south of DS (DS$_P$) and along the ISR slope between Iceland and the Faroe

335 Islands (ISR$_P$) within the $1,000$ and $2,000\ m$ isobath and is followed by a continuous decrease in salinity until $53°N$. The major salinity increase is reached at depths mostly shallower than $600\ m$ for both categories and implies mixing with the ambient upper AMOC water (Figure A4). Due to the shallowness of the overflows over the GSR the mixing of the source NADW water parcels with warmer and more saline upper AMOC waters just south of the overflows is not surprising. After this strong

entrainment at rather shallow depths, the NADW spreads southward along isopycnals that increase their depth towards the

340 south. Due to this relative sinking and the physical properties of the boundary current, some more diapycnal mixing (between $1,000$ and $1,500\ m$), less intense than near the GSR, occurs along the east and west Greenland slopes. Further enhanced mixing is found south and west of Cape Farewell around the Eirik Ridge at depths between $1,500$ and $2,000\ m$, which results in further lightening of the DS_P and ISR_P within the NADW density range.

4 Discussion

345 With 48% of the total NADW and LSW transport the DIA_P represent the majority of NADW (LSW) at $53°N$ in this experiment, which is in alignment with the results of Lumpkin et al. (2008) and Marsh et al. (2005). They found that most of the LSW, leaving the SPNA southward, originate from diapycnal mixing rather than directly from the mixed layer as a result of air–sea fluxes. The DIA_P contributing to the NADW transport at $53°N$ are majorly confined to the continental shelf break (Figure 2 a). Only small diapycnal mass flux is visible in the central Labrador Sea possibly due to mixing induced through eddies

350 shed at Cape Desolation and even smaller, non significant numbers are found in the basin interiors of the Irminger Sea or the Iceland basin (Figure 2 a) (Prater, 2002; Hátún et al., 2007; Rieck et al., 2018). This pattern of densification along the buoyant boundary currents is shown in multiple idealised and realistic model studies (Spall, 2004; Xu et al., 2018; Katsman et al., 2018; Brüggemann and Katsman, 2019; Georgiou et al., 2019; Sidorenko et al., 2020), as well as in observations (Waterhouse et al., 2014). Katsman et al. (2018) show that sinking of water masses occurs where friction plays an important role, thus close

355 to the continental boundary. However, they only consider downwelling in depth space, thus the net sinking is not necessarily associated with a change in density. Based on an idealised model, Brüggemann and Katsman (2019) showed that densification can also be related to transport of water masses from lower to higher densities within the boundary current. In this case water masses are advected laterally across an isopycnal, leading to a change in density. The true causes of this pattern, however, need to be explored in more detail in order to elaborate a profound hypothesis, based on the model's abilities. Here, the densification

360 is understood as a result of diapycnal volume fluxes and mixing induced by strong density gradients in the vicinity of steep topographic slopes and a respective enhanced eddy activity (Spall, 2001; Radko and Marshall, 2004; MacKinnon et al., 2013; Zhang et al., 2019). Consequently, the relative contribution of the basin interiors is negligible as we showed. Additionally, the diapycnal volume fluxes could be further linked to air-sea heat fluxes upstream of the respective NADW origin region through outcropping of the respective isopycnal (Walin, 1982; Grist et al., 2009; Marsh, 2000; Desbruyères et al., 2019; Petit et al.,

365 2020, 2021). The arising density compensated shifts in temperature and salinity in the subpolar mode water (SPMW) just above the NADW could then facilitate densification along the net sinking pathways of SPMW, though this analysis is beyond the scope of this paper. Another aspect of diapycnal mixing is featured in the property change of DS_P and ISR_P, the warming and salinification, from the GSR to $53°N$. These water parcels spread below the main thermocline and gain buoyancy during their southward propagation as expected (MacKinnon et al., 2013). We showed that the major part of the density decrease,

370 at least 50% of the salinification and warming, occurs south of the GSR sills (Figure A4). Here, the mixing driving this density transformation is elevated due to enhanced turbulence through the high velocities (exceeding $20\ cm\ s^{-1}$ reaching up

to $50\ cm\ s^{-1}$) at the sills and the sloping topography (Rudels et al., 2002; Koszalka et al., 2013; Garabato et al., 2019). This is in agreement with the results of Fogelqvist et al. (2003) and Devana et al. (2021), who find a massive impact of upper ocean properties on the NADW passing the GSR channels due to high spill velocities enhancing shear instabilities towards the
375 overlaying upper AMOC waters. South of DS, additionally to the upper AMOC waters, fresh and cold East Greenland Current water is another possible ambient water mass to be entrained (Dickson and Brown, 1994). Hence, we conclude in concurrence with Jochumsen et al. (2015) and Devana et al. (2021) that changes in the mixing ratio and the respective water properties of entrained waters can influence the downstream NADW properties stemming from the GSR majorly. During the spreading along the boundaries a net sinking in depth space of the NADW from the GSR is found (Figure 5 e-f), in correspondence
380 to Katsman et al. (2018). For DIA$_P$ we found a cooling and freshening between the source and target section. Mixing with colder and fresher water from the basin interior could play a role here (Spall and Pickart, 2003). ML$_P$ only show small property alterations along their spreading pathways probably induced through the spatial closeness to the $53°N$ target section.

The mixed layer (ML$_P$) origins contributing majorly to the $53°N$ transport are located within the central Labrador Sea and the Western Boundary Current region in the Labrador Sea (Figure 2 b and Table 2). This is consistent with previous studies,
385 both observational and model–based (Pickart et al., 1997; Marshall and Schott, 1999; Pickart et al., 2002; Cuny et al., 2005; Brandt et al., 2007; MacGilchrist et al., 2020; Georgiou et al., 2021). Here, the contribution from the boundary regions exceed the direct contribution from the interior ($3.3\ Sv$ (46%) compared to $2.6\ Sv$ (36%)). In agreement with Koelling et al. (2022) the export of these ML$_P$ at $53°N$ is between February and April and the transit times between formation and export are only a few months (Figure 5 b). The experiments also show a small but noticeable contribution from the Irminger Sea and from
390 south–east of Cape Farewell (Table 2 and 1). Contributions from these regions are to be expected, since the Irminger Sea and the southern tip of Greenland have been established as additional sites of deep convection (Pickart et al., 2003; Våge et al., 2008; de Jong et al., 2012, 2018; Rühs et al., 2021), although the relative importance of each of them is still under debate. However, the Irminger Sea only plays a minor role in the presented experiments, providing only $1.0\ Sv$ (14%) of the total volume transport associated with the mixed layer, compared to $5.9\ Sv$ (82%) from the Labrador Sea (Table 2). As Rühs et al.
395 (2021) showed, the convection area and density and hence the convective volume produced in the Irminger Sea is comparable to the Labrador Sea in the period 2015-2018. Here, we analyse the period 2010-2019 which is not regarding the possible strong inter-annual variations in relative contribution of the two basins to the overall mixed layer contribution to the NADW at $53°N$. Hence, it is possible that the Irminger Sea contribution is underestimated in the second half of our experiment. Furthermore, in accordance to Le Bras et al. (2020) and Rühs et al. (2021), the shallower components of convective water masses from the
400 Irminger Sea tend to be lighter compared to water masses formed within the Labrador Sea (Figure A1). Thus, it is possible that particles leaving the mixed layer in the Irminger Sea undergo further transformation along their pathways towards $53°N$. If these particles experience a reduction in density to values lower than σ_{DW} they would add volume to the SPMW but not to the NADW and are not covered in our experiment. On the other hand, if the density is increased to values higher than σ_{DW} again at a later point, these particles would be attributed to a different region or a different source entirely.
405 Overall, at $53°N$ the total Labrador Sea contribution ($5.9\ Sv$) to the formation of NADW dominates over the Irminger Sea contribution ($1.0\ Sv$) for the evaluated experiment period (Table 2). This seems to be in contrast with recent observation–based

studies. Lozier et al. (2019) state that OSNAP East dominates the AMOC in the SPNA, rather than OSNAP West. The study by Bower et al. (2009) shows that interior pathways are likely to be at least equally important for the export of NADW from the SPNA. The experiments presented here only take into account the volume transport at $53°N$, i.e. the NADW export within

410 the DWBC. Thus, here we do not represent the relative contribution of each basin to the total SPNA NADW southward export, which would reflect the AMOC.

Due to our experimental setup and as expected from literature (Kieke and Yashayaev, 2015; Palter et al., 2016; Fischer et al., 2018), NADW is majorly advected within the boundary currents close to the continental slope or the shelf break. Already west of the Eirik Ridge we noticed an enhanced divergence of the particle pathways, which coincides with trajectories from

415 RAFOS floats of the OSNAP float program (Zou et al., 2021). Near Cape Desolation the pathways further diverge into the Labrador Sea, becoming less confined due to bifurcation and the shedding of Irminger Rings (Cuny et al., 2002; Prater, 2002; Hátún et al., 2007; Higginson et al., 2011; Palter et al., 2016; Rieck et al., 2018). Thus, water parcels are transported along more diverse pathways from Greenland across the Labrador Sea before joining into the more confined DWBC off Labrador. South of $53°N$ all particle categories also feature a re–circulation cell around Orphan Knoll in agreement with previous studies

420 (Lavender et al., 2000; Xu et al., 2010). Hence, a slight NADW volume formation is also possible south of $53°N$ possibly due to horizontal mixing or ocean-atmosphere interaction. These waters can then recirculate to $53°N$ and the Labrador Sea.

Concerning the volume transports our results are only faintly comparable to existing literature. Usually, the transports at $53°N$ are classified after their water mass properties into LSW, NEADW and DSOW which are of course related to their origins and have defined properties in temperature, salinity, density and/or potential vorticity (Zantopp et al., 2017; Liu and

425 Tanhua, 2021). Here, we did not define rigid density classes but classified the transport volumes after their specific formation origin. Our experiments reveal that the specific particle categories are not primarily linked to an overall density definition at $53°N$ but rather to a similar formation region in combination with a specific transformation history. Just like the classical understanding of water masses, the densities are ordered with the densest components at origin at the ISR ($\sigma_0 = 28.05 \; kg \; m^{-3}$) and DS ($\sigma_0 = 27.98 \; kg \; m^{-3}$ and $\sigma_0 = 27.87 \; kg \; m^{-3}$), and the lightest component from the mixed layer ($\sigma_0 = 27.75 \; kg \; m^{-3}$

430). In the classical view, the diapycnal component would be associated with one of these origins, as e.g an increase in overflow volume south of the sills. But here, due to the water mass definitions in the model only the minorly transformed water from the GSR would be associated with DSOW and NEADW. Since we find most of the transport originating from the GSR contributes to LSW instead of lNADW within the here applied definitions (Handmann et al., 2018) the relative contribution of LSW and lNADW in our experiment does not concur with a transport distribution of $\sim 50{:}50$ between LSW (14.9 ± 3.9 Sv) and lNADW

435 (15.3 ± 3.8) at $53°N$ found by Zantopp et al. (2017) for the period 1997-2014. Further upstream at the GSR, the Eulerian transports of the overflow components of the used model VIKING20X-JRA-OMIP and the observations were compared in Biastoch et al. (2021) and found very similar. This coincides with the total NADW sourced at DS ($3.8 \; Sv$) found in this experiment. As mentioned by Zou et al. (2020b) and Bower and Furey (2017) the water stemming from the ISR can spread following very diffusive pathways. As we are only sampling water parcels passing $53°N$, the $1.9 \; Sv$ stemming from the ISR

440 seem to be reasonable. From an observational point of view, the volume of the overflow water masses ($\sim 5 \; Sv$ at the sills) is largely increased due to entrainment of ambient water masses along its southward spreading ($\sim 15 \; Sv$ at $53°N$) (Hansen

et al., 2003; Zantopp et al., 2017). Hence, these additional $\sim 10\,Sv$ are most probably represented in the DIA_P water class in our experiments. On the other hand, in our experiment, the densest water below $\sigma_0 = 27.86\,kg\,m^{-3}$ cannot be assigned to a specific source after 40 years of advection. Most probably, this dense water is introduced at the initialisation of the model and

445   not refreshed or majorly changed and rather reduced towards lighter densities during the model run. Pathways of RES_P are concentrated west of the Mid–Atlantic Ridge. This is related to the fact that the residuum mostly contains particles with very high densities that re–circulate within the western SPNA, and are unable to cross the Mid–Atlantic Ridge. To conclude, we find that the density interval with the major transports in NADW at $53°N$ around $\sigma_2 = 27.80\,kg\,m^{-3}$ is not only associated with one source. Instead multiple sources contribute with different relative importance to similar density regimes, though the

450   DIA_P and ML_P dominate (Figure 3).

5   Conclusion

In order to assess the mean relative contributions of the different sources of NADW passing the southern exit of the Labrador Sea at $53°N$, Lagrangian particle experiments were conducted in the high-resolution ocean model VIKING20x-JRA-OMIP. Each particle represents a defined volume and retains it along its trajectory, similar to stream tubes in a steady flow (van Sebille

455   et al., 2017). Since the volume of each particle is preserved, but its properties are allowed to change along its trajectory, this resulted in the evaluation of the various sources, pathways, advection time scales and property transitions that NADW water parcels are subject to during their spreading from their origin in the SPNA to $53°N$.

In this study we show the multiple sources of NADW passing $53°N$ contributing to similar density regimes. The classical view of density classes being directly linked to a common formation region holds only partly within our experiments. We rather

460   find that different origins in combination with transformation processes such as diapycnal mixing along the pathways lead to water mass properties that can be very similar at the southern exit of the Labrador Sea. We found that water passing the GSR (DS_P, ISR_P) within the NADW layer lightens within the NADW class through warming and salinification just south of the sills by mixing with ambient water. Contrary, NADW water originating from densification through diapycnal mixing (DIA_P) or contact with the mixed layer (ML_P) rather densifies after entering the NADW density class through cooling and freshening.

465   Due to our focus on the NADW transport within the DWBC at $53°N$, in our experiments the volume contribution from the Labrador Sea dominates over the rest of the subpolar North Atlantic. Since we analyzed our experiment in an averaging manner for the period 2010-2019 the inter-annual variability of the different sources is not discussed here. The relative importance of origin regions and transformation processes over time is hence a topic left for further analysis.

Data availability.   The trajectory data, analyzed in the current study are available from the corresponding authors on request.

470   *Author contributions.* PH and AB defined and guided the overall research problem and methodology. JF developed and performed the Lagrangian experiments and did the analyses and figures. JF and PH wrote the manuscript. All co-authors discussed the analyses and contributed to the text. The authors declare that they have no conflict of interest. All authors agree to be accountable for the content of the work.

Competing interests. The authors declare that the research was conducted in the absence of any commercial or financial relationships that
475   could be construed as a potential conflict of interest.

Acknowledgements. We thank Dr. Willi Rath for the support during the experimental setup. We thank Dr. Franziska Schwarzkopf for running the Viking20x-JRA-OMIP model. This work received support by the Initiative and Networking Fund of the Helmholtz Association through the project "Advanced Earth System Modelling Capacity (ESM)"

Appendix A: Supplementary Figures
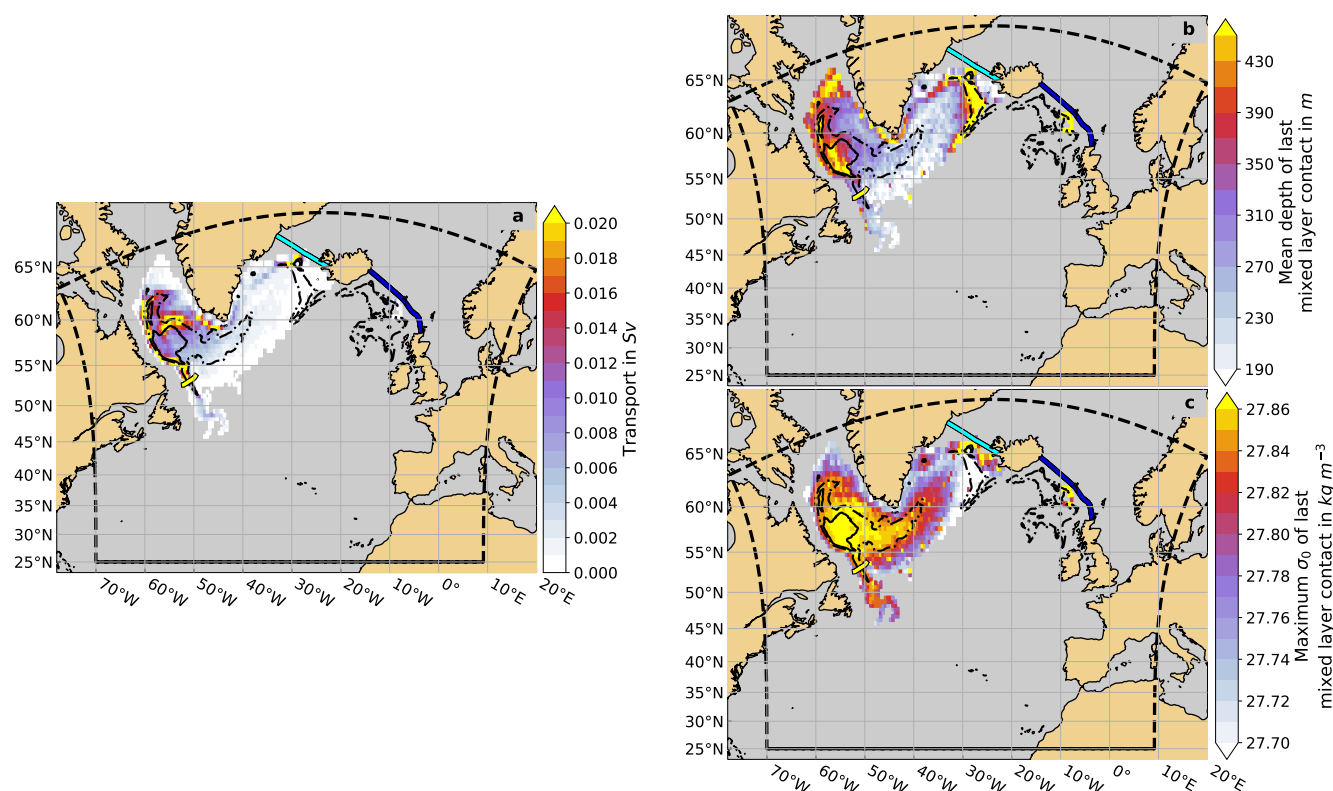
Figure A1. (a) Locations of origin, calculated as mean transport in Sv (shading, $1/2° \times 1/2°$ bins) for ML_P (see section 2.2 for details of the definitions). (b-c) Transport–weighted mean depth in m (b) and maximum σ_0 in $kg\ m^{-3}$ (c) of last mixed layer contact per $1/2° \times 1/2°$ bin for ML_P. The black solid contour marks the 2000-2019 mean DJFM mixed layer depth of $500\ m$. The black dash–dotted contour marks the 2000-2019 mean of the annual maximum mixed layer depth of $500\ m$. The yellow line marks the $53°N$ section, the light and dark blue lines mark the Denmark Strait and Iceland–Scotland Ridge sections, respectively. The black dashed line indicates the boundary of the experiment domain.
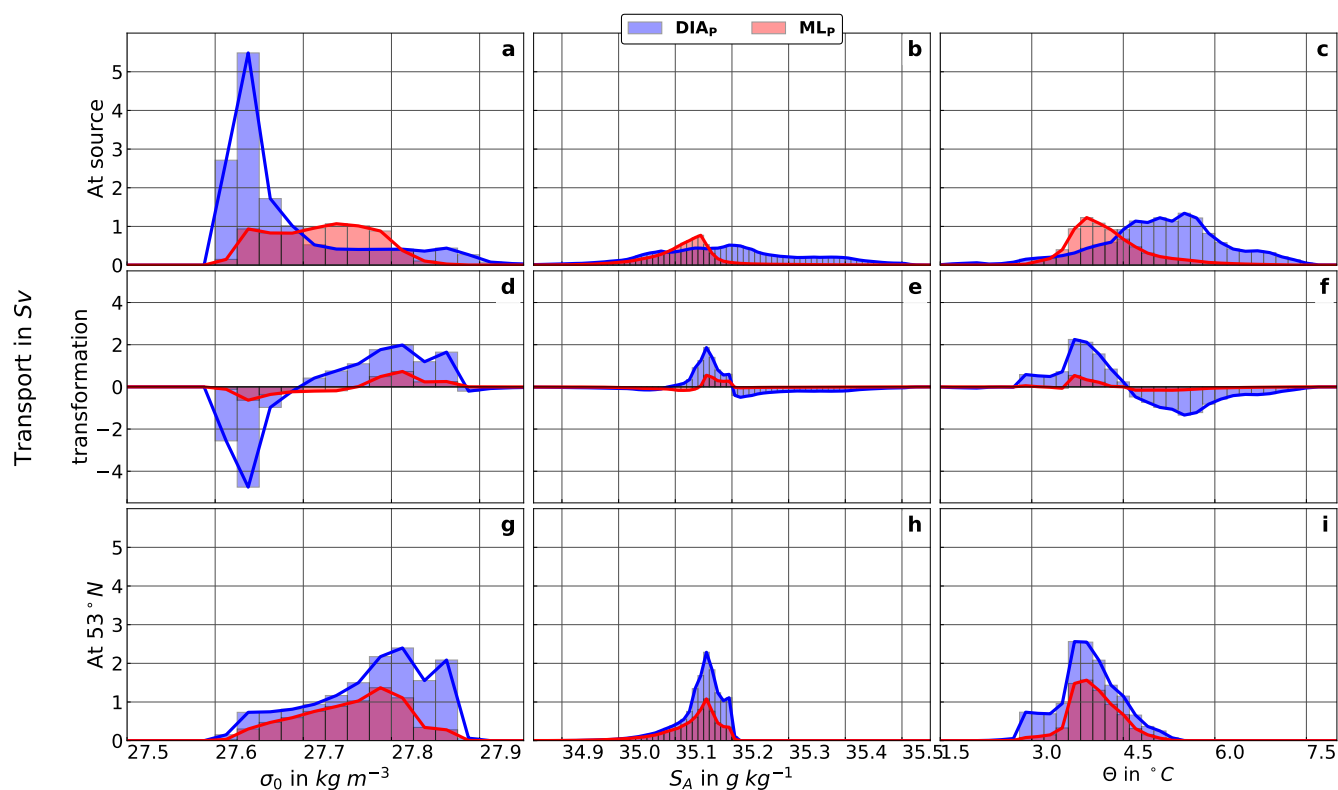
Figure A2. Mean water mass property modifications for DIA$_P$ (blue) and ML$_P$ (red) (see section 2.2 for details of the definitions). Shown are mean volume transport in Sv per potential density (referenced to $0\ dbar$, σ_0) ((a, d, g), $0.025\ kg\ m^{-3}$ bins), absolute salinity (S_A) ((b, e, h), $0.01\ g\ kg^{-1}$ bins) and conservative temperature (Θ) ((c, f, i), $0.2°C$ bins) class at their source region ((a to c)) and at $53°N$ ((g to i)), as well as the volumetric property transformation ((d to f)).
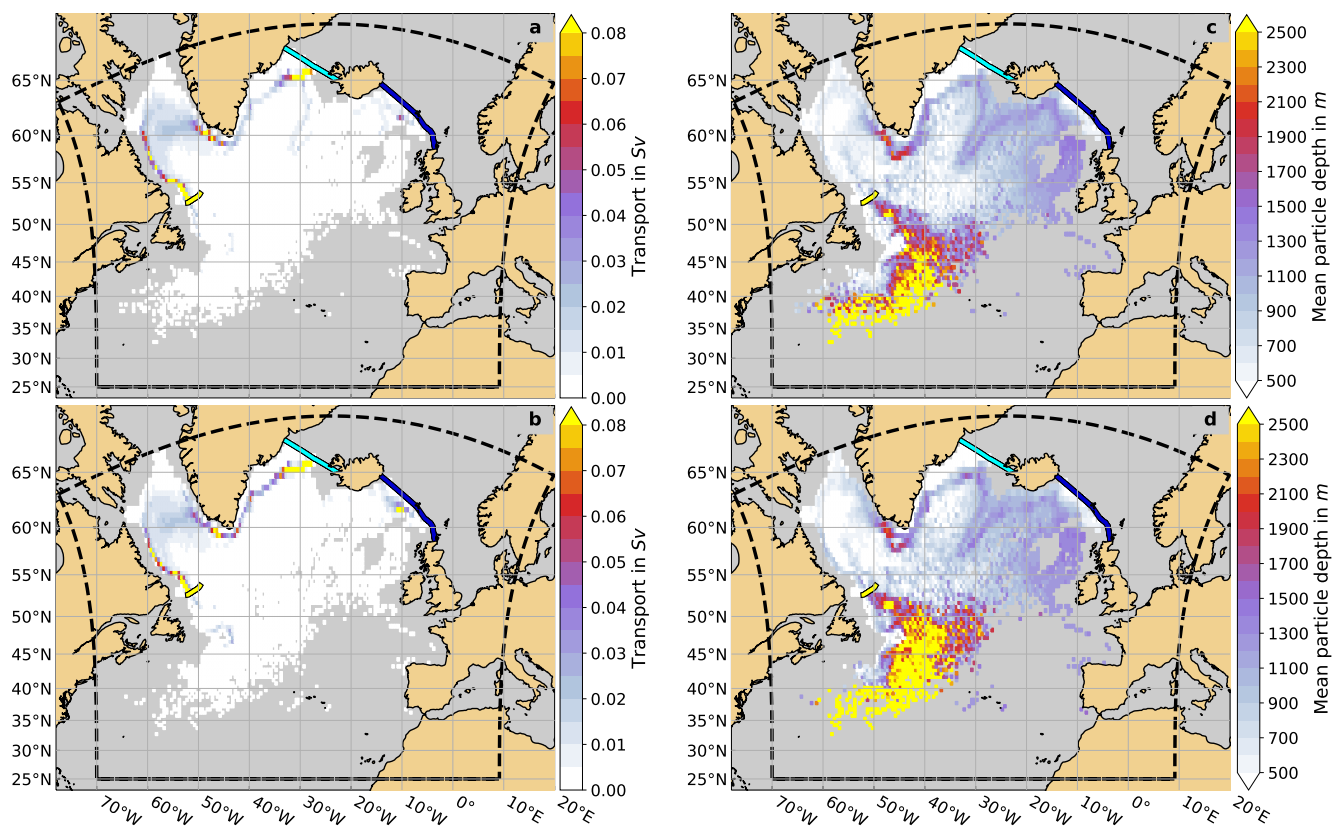
Figure A3. (a-b) Locations associated with most transport in Sv and (c-d) mean particle depth in m per $1/2° \times 1/2°$ bin. The particle locations are chosen as the locations where the difference in salinity between the particle's salinity minimum and its source is halved (a, c) and where the difference in temperature between the particle's temperature minimum and its source is halved (b, d). The yellow line marks the $53°N$ section, the light and dark blue lines mark the Denmark Strait and Iceland–Scotland Ridge sections, respectively. The black dashed line indicates the boundary of the experiment domain.
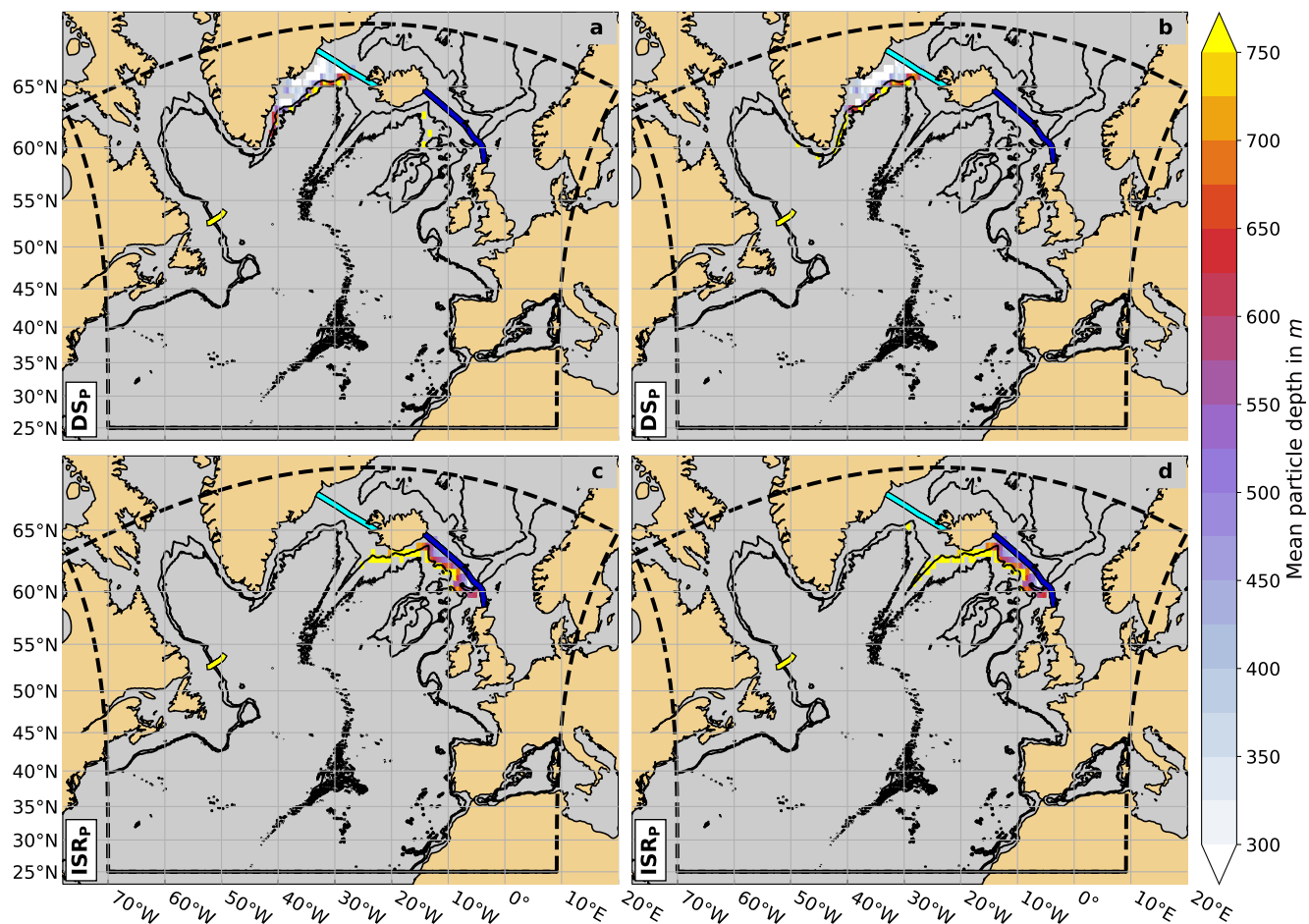
Figure A4. Mean depth of major (a, c) salinity and (b, d) temperature increase for DS$_P$ (a, b) and ISR$_P$ (c, d), calculated as the transport–weighted mean particle depth in m per $1/2° \times 1/2°$ bin. The particle locations are chosen as the locations where the difference in salinity between the particle's salinity maximum and its source is halved (a, c) and where the difference in temperature between the particle's temperature maximum and its source is halved (b, d). Black contours mark the $1,000$ and $2,000$ m isobaths. The yellow line marks the $53°N$ section, the light and dark blue lines mark the Denmark Strait and Iceland–Scotland Ridge sections, respectively. The black dashed line indicates the boundary of the experiment domain.
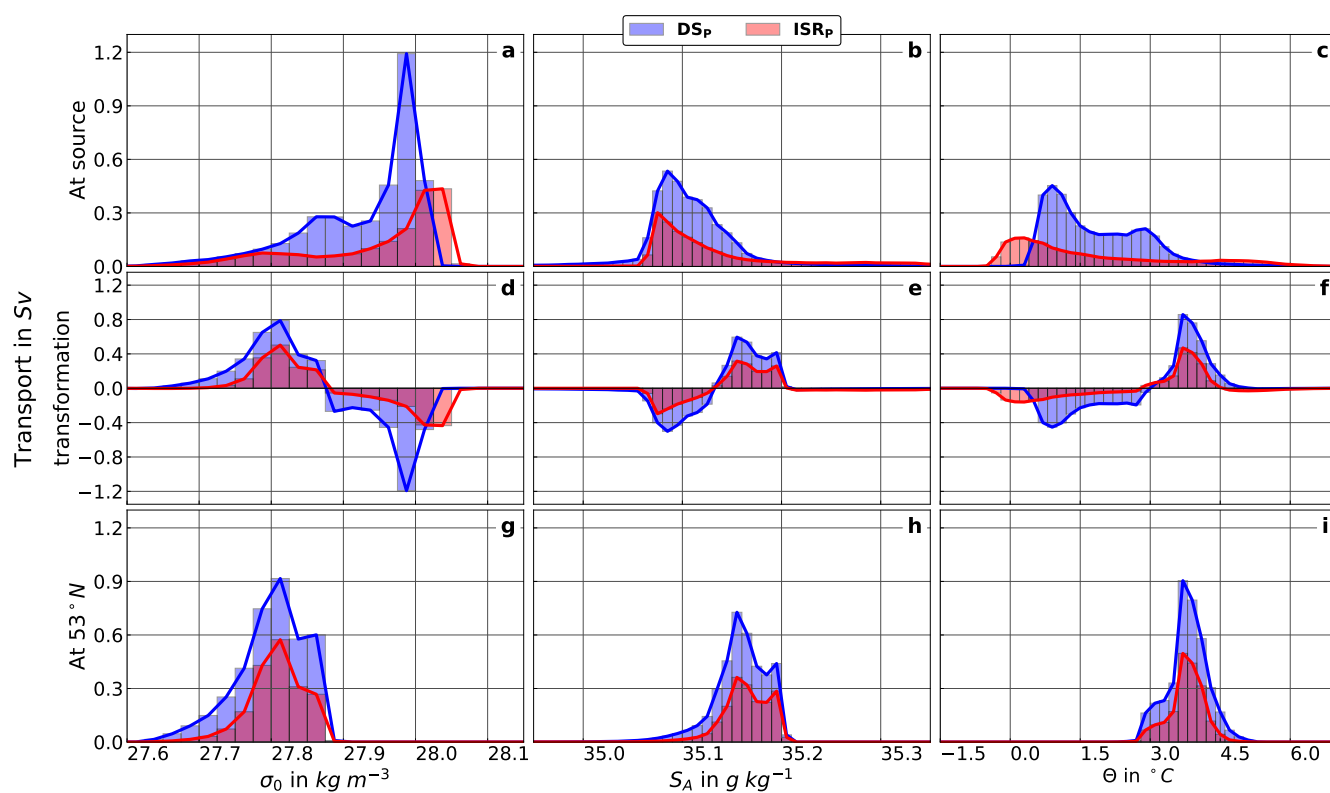
Figure A5. As in Figure A2, but for DS_P (blue) and ISR_P (red) (see section 2.2 for details of the definitions).

References

Berx, B., Hansen, B., Østerhus, S., Larsen, K., Sherwin, T., and Jochumsen, K.: Combining in-situ measurements and altimetry to estimate volume, heat and salt transport variability through the Faroe Shetland Channel, Ocean Science Discussions, 10, 153–195, doi:10.5194/os-9-639-2013, 2013.

Biastoch, A., Schwarzkopf, F. U., Getzlaff, K., Rühs, S., Martin, T., Scheinert, M., Schulzki, T., Handmann, P., Hummels, R., and Böning, C. W.: Regional Imprints of Changes in the Atlantic Meridional Overturning Circulation in the Eddy-rich Ocean Model VIKING20X, Ocean Science Discussions, pp. 1–52, 2021.

Bower, A. S. and Furey, H.: Iceland-Scotland Overflow Water transport variability through the Charlie-Gibbs Fracture Zone and the impact of the North Atlantic Current, Journal of Geophysical Research: Oceans, 2017.

Bower, A. S., Lozier, M. S., Gary, S. F., and Böning, C. W.: Interior pathways of the North Atlantic meridional overturning circulation, Nature, 459, 243–247, http://www.nature.com/nature/journal/v459/n7244/abs/nature07979.html, 2009.

Brandt, P., Funk, A., Czeschel, L., Eden, C., and Böning, C. W.: Ventilation and transformation of Labrador Sea Water and its rapid export in the deep Labrador Current, Journal of physical oceanography, 37, 946–961, 2007.

Brüggemann, N. and Katsman, C. A.: Dynamics of downwelling in an eddying marginal sea: contrasting the Eulerian and the isopycnal perspective, Journal of Physical Oceanography, 49, 3017–3035, 2019.

Cuny, J., Rhines, P. B., Niiler, P. P., and Bacon, S.: Labrador Sea boundary currents and the fate of the Irminger Sea Water, Journal of Physical Oceanography, 32, 627–647, 2002.

Cuny, J., Rhines, P. B., Schott, F., and Lazier, J.: Convection above the Labrador continental slope, Journal of Physical Oceanography, 35, 489–511, 2005.

de Jong, M. F., van Aken, H. M., Våge, K., and Pickart, R. S.: Convective mixing in the central Irminger Sea: 2002–2010, Deep Sea Research Part I: Oceanographic Research Papers, 63, 36–51, 2012.

de Jong, M. F., Oltmanns, M., Karstensen, J., and de Steur, L.: Deep convection in the Irminger Sea observed with a dense mooring array, Oceanography, 31, 50–59, 2018.

Delandmeter, P. and Sebille, E. v.: The Parcels v2. 0 Lagrangian framework: new field interpolation schemes, Geoscientific Model Development, 12, 3571–3584, 2019.

Desbruyères, D. G., Mercier, H., Maze, G., and Daniault, N.: Surface predictor of overturning circulation and heat content change in the subpolar North Atlantic, Ocean Sci., 15, 809–817, https://www.ocean-sci.net/15/809/2019/, 2019.

Devana, M. S., Johns, W. E., Houk, A., and Zou, S.: Rapid Freshening of Iceland Scotland Overflow Water Driven By Entrainment of a Major Upper Ocean Salinity Anomaly, Geophysical Research Letters, 48, e2021GL094 396, https://doi.org/https://doi.org/10.1029/2021GL094396, 2021.

Dickson, R. R. and Brown, J.: The production of North Atlantic Deep Water: sources, rates, and pathways, Journal of Geophysical Research: Oceans (1978–2012), 99, 12 319–12 341, 1994.

Dietrich, G.: Ozeanographische Probleme der deutschen Forschungsfahrten im Internationalen Geophysikalischen Jahr 1957/58, Deutsche Hydrografische Zeitschrift, 10, 39–61, 1957.

Fichefet, T. and Maqueda, M. A.: Sensitivity of a global sea ice model to the treatment of ice thermodynamics and dynamics, Journal of Geophysical Research: Oceans, 102, 12 609–12 646, 1997.

Fischer, J., Karstensen, J., Oltmanns, M., and Schmidtko, S.: Mean circulation and EKE distribution in the Labrador Sea Water level of the subpolar North Atlantic, Ocean Science Discussions, pp. 1–27, 2018.

Fogelqvist, E., Blindheim, J., Tanhua, T., Østerhus, S., Buch, E., and Rey, F.: Greenland-Scotland overflow studied by hydro-chemical multivariate analysis, Deep Sea Research Part I: Oceanographic Research Papers, 50, 73–102, http://www.sciencedirect.com/science/article/pii/S0967063702001310, 2003.

Fröb, F., Olsen, A., Våge, K., Moore, G. W. K., Yashayaev, I., Jeansson, E., and Rajasakaren, B.: Irminger Sea deep convection injects oxygen and anthropogenic carbon to the ocean interior, Nature communications, 7, 1–8, 2016.

Garabato, A. C. N., Frajka-Williams, E. E., Spingys, C. P., Legg, S., Polzin, K. L., Forryan, A., Abrahamsen, E. P., Buckingham, C. E., Griffies, S. M., and McPhail, S. D.: Rapid mixing and exchange of deep-ocean waters in an abyssal boundary current, Proceedings of the National Academy of Sciences, 116, 13 233–13 238, 2019.

Georgiou, S., van der Boog, C. G., Brüggemann, N., Ypma, S. L., Pietrzak, J. D., and Katsman, C. A.: On the interplay between downwelling, deep convection and mesoscale eddies in the Labrador Sea, Ocean Modelling, 135, 56–70, http://www.sciencedirect.com/science/article/pii/S1463500318303032, 2019.

Georgiou, S., Ypma, S. L., Brüggemann, N., Sayol, J.-M., Pietrzak, J. D., and Katsman, C. A.: Pathways of the water masses exiting the Labrador Sea: The importance of boundary-interior exchanges, Ocean Modelling, p. 101623, 2020.

Georgiou, S., Ypma, S. L., Brüggemann, N., Sayol, J.-M., van der Boog, C. G., Spence, P., Pietrzak, J. D., and Katsman, C. A.: Direct and Indirect Pathways of Convected Water Masses and Their impacts on the Overturning Dynamics of the Labrador Sea, J. Geophys. Res. Oceans, 126, e2020JC016 654, https://doi.org/10.1029/2020JC016654, 2021.

Grist, J. P., Marsh, R., and Josey, S. A.: On the relationship between the North Atlantic meridional overturning circulation and the surface-forced overturning streamfunction, Journal of Climate, 22, 4989–5002, http://journals.ametsoc.org/doi/abs/10.1175/2009JCLI2574.1, 2009.

Haine, T., Böning, C., Brandt, P., Fischer, J., Funk, A., Kieke, D., Kvaleberg, E., Rhein, M., and Visbeck, M.: North Atlantic deep water formation in the Labrador Sea, recirculation through the subpolar gyre, and discharge to the subtropics, in: Arctic - Subarctic Ocean Fluxes, pp. 653–701, Springer, 2008.

Handmann, P.: Deep Water Formation and Spreading Dynamics in the subpolar North Atlantic from Observations and high-resolution Ocean Models, Ph.D. thesis, Christian-Albrechts-Universität Kiel, 2019.

Handmann, P., Fischer, J., Visbeck, M., Karstensen, J., Biastoch, A., Böning, C., and Patara, L.: The Deep Western Boundary Current in the Labrador Sea From Observations and a High-Resolution Model, Journal of Geophysical Research: Oceans, 2018.

Hansen, B., Østerhus, S., Hátún, H., Kristiansen, R., and Larsen, K. M. H.: The Iceland-Faroe inflow of Atlantic water to the Nordic Seas, Progress in Oceanography, 59, 443–474, http://www.sciencedirect.com/science/article/pii/S0079661103001770, 2003.

Hansen, B., Larsen, H., Margretha, K., Hátún, H., and Østerhus, S.: A stable Faroe Bank Channel overflow 1995–2015, Ocean Science, 12, 1205–1220, 2016.

Hansen, B. and Østerhus, S.: North atlantic–nordic seas exchanges, Progress in Oceanography, 45, 109–208, 2000.

Harden, B. E., Pickart, R. S., Valdimarsson, H., Våge, K., de Steur, L., Richards, C., Bahr, F., Torres, D., Børve, E., and Jónsson, S.: Upstream sources of the Denmark Strait Overflow: Observations from a high-resolution mooring array, Deep Sea Research Part I: Oceanographic Research Papers, 112, 94–112, 2016.

Hátún, H., Eriksen, C. C., and Rhines, P. B.: Buoyant eddies entering the Labrador Sea observed with gliders and altimetry, Journal of Physical Oceanography, 37, 2838–2854, 2007.

Higginson, S., Thompson, K., Huang, J., Véronneau, M., and Wright, D.: The mean surface circulation of the North Atlantic subpolar gyre: A comparison of estimates derived from new gravity and oceanographic measurements, Journal of Geophysical Research: Oceans, 116, 2011.

Hjartarson, A., Erlendsson, Ö., and Blischke, A.: The Greenland–Iceland–Faroe Ridge Complex, Geological Society, London, Special Publications, 447, 127–148, https://doi.org/10.1144/SP447.14, 2017.

Intergovernmental Oceanographic Commission: The International thermodynamic equation of seawater–2010: calculation and use of thermodynamic properties.[includes corrections up to 31st October 2015]., 2015.

Jochumsen, K., Köllner, M., Quadfasel, D., Dye, S., Rudels, B., and Valdimarsson, H.: On the origin and propagation of Denmark Strait overflow water anomalies in the Irminger Basin, Journal of Geophysical Research: Oceans, 120, 1841–1855, 2015.

Jochumsen, K., Moritz, M., Nunes, N., Quadfasel, D., Larsen, K. M. H., Hansen, B., Valdimarsson, H., and Jonsson, S.: Revised transport estimates of the D enmark S trait overflow, Journal of Geophysical Research: Oceans, 122, 3434–3450, 2017.

Johnson, G. C., Purkey, S. G., Zilberman, N. V., and Roemmich, D.: Deep Argo Quantifies Bottom Water Warming Rates in the Southwest Pacific Basin, Geophys. Res. Lett., 46, 2662–2669, https://doi.org/10.1029/2018gl081685, 2019.

Jong, M. F. and Steur, L.: Strong winter cooling over the Irminger Sea in winter 2014-2015, exceptional deep convection, and the emergence of anomalously low SST, Geophysical Research Letters, 2016.

Katsman, C., Drijfhout, S., Dijkstra, H., and Spall, M.: Sinking of Dense North Atlantic Waters in a Global Ocean Model: Location and Controls, Journal of Geophysical Research: Oceans, 2018.

Kieke, D. and Yashayaev, I.: Studies of Labrador Sea Water formation and variability in the subpolar North Atlantic in the light of international partnership and collaboration, Progress in Oceanography, 132, 220–232, 2015.

Koelling, J., Atamanchuk, D., Karstensen, J., Handmann, P., and Wallace, D. W. R.: Oxygen export to the deep ocean following Labrador Sea Water formation, Biogeosciences, 19, 437–454, 2022.

Koszalka, I. M., Haine, T. W. N., and Magaldi, M. G.: Fates and Travel Times of Denmark Strait Overflow Water in the Irminger Basin, Journal of Physical Oceanography, 43, 2611–2628, https://doi.org/10.1175/JPO-D-13-023.1, 2013.

Lab Sea Group: The Labrador Sea deep convection experiment, Bulletin of the American Meteorological Society, 79, 2033–2058, 1998.

Lankhorst, M. and Zenk, W.: Lagrangian observations of the middepth and deep velocity fields of the northeastern Atlantic Ocean, Journal of physical oceanography, 36, 43–63, 2006.

Lavender, K. L., Davis, R. E., and Owens, W. B.: Mid-depth recirculation observed in the interior Labrador and Irminger Seas by direct velocity measurements, Nature, 407, 66–69, 2000.

Lazier, J.: The renewal of Labrador Sea water, in: Deep Sea Research and Oceanographic Abstracts, vol. 20, pp. 341–353, Elsevier, 1973.

Le Bras, I. A.-A., Straneo, F., Holte, J., de Jong, M. F., and Holliday, N. P.: Rapid Export of Waters Formed by Convection Near the Irminger Sea's Western Boundary, Geophys. Res. Lett., 47, e2019GL085 989, https://doi.org/10.1029/2019gl085989, 2020.

Lilly, J. M., Rhines, P. B., Schott, F., Lavender, K., Lazier, J., Send, U., and D'Asaro, E.: Observations of the Labrador Sea eddy field, Progress in Oceanography, 59, 75–176, 2003.

Liu, M. and Tanhua, T.: Water masses in the Atlantic Ocean: characteristics and distributions, Ocean Science, 17, 463–486, 2021.

Lozier, M. S.: Overturning in the North Atlantic, Annual review of marine science, 4, 291–315, http://www.annualreviews.org/doi/abs/10.1146/annurev-marine-120710-100740, 2012.

590 Lozier, M. S., Bacon, S., Bower, A. S., Cunningham, S. A., Femke de Jong, M., De Steur, L., Deyoung, B., Fischer, J., Gary, S. F., and Greenan, B. J. W.: Overturning in the Subpolar North Atlantic Program: a new international ocean observing system, Bulletin of the American Meteorological Society, 98, 737–752, 2017.

Lozier, M. S., Li, F., Bacon, S., Bahr, F., Bower, A. S., Cunningham, S. A., de Jong, M. F., de Steur, L., deYoung, B., Fischer, J., Gary, S. F.,
595   Greenan, B. J. W., Holliday, N. P., Houk, A., Houpert, L., Inall, M. E., Johns, W. E., Johnson, H. L., Johnson, C., Karstensen, J., Koman, G., Le Bras, I. A., Lin, X., Mackay, N., Marshall, D. P., Mercier, H., Oltmanns, M., Pickart, R. S., Ramsey, A. L., Rayner, D., Straneo, F., Thierry, V., Torres, D. J., Williams, R. G., Wilson, C., Yang, J., Yashayaev, I., and Zhao, J.: A sea change in our view of overturning in the subpolar North Atlantic, Science, 363, 516, http://science.sciencemag.org/content/363/6426/516.abstract, 2019.

Lumpkin, R., Speer, K. G., and Koltermann, K. P.: Transport across 48 N in the Atlantic Ocean, Journal of Physical Oceanography, 38, 733–752, 2008.

600 MacGilchrist, G. A., Johnson, H. L., Marshall, D. P., Lique, C., Thomas, M., Jackson, L. C., and Wood, R. A.: Locations and mechanisms of ocean ventilation in the high-latitude North Atlantic in an eddy-permitting ocean model, Journal of Climate, pp. 1–61, 2020.

MacKinnon, J., St Laurent, L., and Naveira Garabato, A. C.: Chapter 7 - Diapycnal Mixing Processes in the Ocean Interior, in: Ocean Circulation and Climate, edited by Siedler, G., Griffies, S. M., Gould, J., and Church, J. A., vol. 103 of *International Geophysics*, pp. 159–183, Academic Press, https://doi.org/https://doi.org/10.1016/B978-0-12-391851-2.00007-6, 2013.

605 Madec, G., Bourdallé-Badie, R., Bouttier, P.-A., Bricaud, C., Bruciaferri, D., Calvert, D., Chanut, J., Clementi, E., Coward, A., Delrosso, D., Ethé, C., Flavoni, S., Graham, T., Harle, J., Iovino, D., Lea, D., Lévy, C., Lovato, T., Martin, N., Masson, S., Mocavero, S., Paul, J., Rousset, C., Storkey, D., Storto, A., and Vancoppenolle, M.: NEMO ocean engine, https://doi.org/10.5281/zenodo.1472492, revision 8625 from SVN repository, 2017.

Marsh, R.: Recent variability of the North Atlantic thermohaline circulation inferred from surface heat and freshwater fluxes, Journal of
610   climate, 13, 3239–3260, 2000.

Marsh, R., De Cuevas, B. A., Coward, A. C., Bryden, H. L., and Álvarez, M.: Thermohaline circulation at three key sections in the North Atlantic over 1985–2002, Geophysical Research Letters, 32, 2005.

Marshall, J. and Schott, F.: Open-ocean convection: Observations, Theory and Models, Reviews of Geophysics, 37, 1–64, 1999.

Molinari, R. L., Fine, R. A., Wilson, W. D., Curry, R. G., Abell, J., and McCartney, M. S.: The arrival of recently formed Labrador Sea Water
615   in the deep western boundary current at 26.5 N, Geophysical Research Letters, 25, 2249–2252, 1998.

Palter, J. B., Caron, C.-A., Law, K. L., Willis, J. K., Trossman, D. S., Yashayaev, I. M., and Gilbert, D.: Variability of the directly observed, middepth subpolar North Atlantic circulation, Geophys. Res. Lett., 43, 2700–2708, https://doi.org/10.1002/2015gl067235, 2016.

Petit, T., Lozier, M. S., Josey, S. A., and Cunningham, S. A.: Atlantic deep water formation occurs primarily in the Iceland Basin and Irminger Sea by local buoyancy forcing, Geophysical Research Letters, 47, e2020GL091 028, 2020.

620 Petit, T., Lozier, M. S., Josey, S. A., and Cunningham, S. A.: Role of air-sea fluxes and ocean surface density on the production of deep waters in the eastern subpolar gyre of the North Atlantic, Ocean Science Discussions, pp. 1–21, 2021.

Pickart, R. S.: Water mass components of the North Atlantic deep western boundary current, Deep Sea Research Part A. Oceanographic Research Papers, 39, 1553–1572, http://www.sciencedirect.com/science/article/pii/019801499290047W, 1992.

Pickart, R. S. and Spall, M. A.: Impact of Labrador Sea Convection on the North Atlantic Meridional Overturning Circulation, J. Phys.
625   Oceanogr., 37, 2207–2227, https://doi.org/10.1175/jpo3178.1, 2007.

Pickart, R. S., Spall, M., and Lazier, J.: Mid-depth ventilation in the western boundary current system of the sub-polar gyre, Deep Sea Research Part I: Oceanographic Research Papers, 44, 1025–1054, 1997.

Pickart, R. S., Torres, D. J., and Clarke, R. A.: Hydrography of the Labrador Sea during active convection, Journal of Physical Oceanography, 32, 428–457, http://journals.ametsoc.org/doi/abs/10.1175/1520-0485(2002)032%3C0428:HOTLSD%3E2.0.CO%3B2, 2002.

630 Pickart, R. S., Spall, M. A., Ribergaard, M. H., Moore, G. W. K., and Milliff, R. F.: Deep convection in the Irminger Sea forced by the Greenland tip jet, Nature, 424, 152, https://doi.org/10.1038/nature01729, 2003.

Piron, A., Thierry, V., Mercier, H., and Caniaux, G.: Argo float observations of basin-scale deep convection in the Irminger sea during winter 2011-2012, Deep Sea Research Part I: Oceanographic Research Papers, 109, 76–90, http://www.sciencedirect.com/science/article/pii/S0967063716000121, 2016.

635 Prater, M. D.: Eddies in the Labrador Sea as observed by profiling RAFOS floats and remote sensing, Journal of Physical Oceanography, 32, 411–427, 2002.

Radko, T. and Marshall, J.: Eddy-Induced Diapycnal Fluxes and Their Role in the Maintenance of the Thermocline, Journal of Physical Oceanography, 34, 372–383, https://doi.org/10.1175/1520-0485(2004)034<0372:EDFATR>2.0.CO;2, 2004.

Rhein, M., Kieke, D., Hüttl-Kabus, S., Roessler, A., Mertens, C., Meissner, R., Klein, B., Böning, C. W., and Yashayaev, I.: Deep water
640   formation, the subpolar gyre, and the meridional overturning circulation in the subpolar North Atlantic, Deep Sea Research Part II: Topical Studies in Oceanography, 58, 1819–1832, http://www.sciencedirect.com/science/article/pii/S0967064511000440, 2011.

Rhein, M., Rintoul, S., Aoki, S., Campos, E., Chambers, D., Feely, R., Gulev, S., Johnson, G., Josey, S., Kostianoy, A., et al.: Observations: ocean, pp. 255–316, Cambridge University Press, https://doi.org/10.1017/CBO9781107415324.010, 2013.

Rieck, J. K., Böning, C., and Getzlaff, K.: The Nature of Eddy Kinetic Energy in the Labrador Sea: Different Types of Mesoscale Eddies,
645   their Temporal Variability and Impact on Deep Convection, Journal of Physical Oceanography, 2018.

Rossby, T., Flagg, C., Chafik, L., Harden, B., and Søiland, H.: A Direct Estimate of Volume, Heat, and Freshwater Exchange Across the Greenland-Iceland-Faroe-Scotland Ridge, Journal of Geophysical Research: Oceans, 123, 7139–7153, 2018.

Rudels, B., Eriksson, P., Fahrbach, E., Budéus, G., and Meincke, J.: The East Greenland Current and its contribution to the Denmark Strait overflow, icesjms, 59, 1133–1154, https://doi.org/10.1006/jmsc.2002.1284, 2002.

650 Rühs, S., Oliver, E. C. J., Biastoch, A., Böning, C. W., Dowd, M., Getzlaff, K., Martin, T., and Myers, P. G.: Changing spatial patterns of deep convection in the subpolar North Atlantic, Journal of Geophysical Research: Oceans, p. e2021JC017245, 2021.

Sayol, J.-M., Dijkstra, H., and Katsman, C.: Seasonal and regional variations of sinking in the subpolar North Atlantic from a high-resolution ocean model, Ocean Science, 15, 1033–1053, https://www.ocean-sci.net/15/1033/2019/, 2019.

Schmidt, C., Schwarzkopf, F. U., Rühs, S., and Biastoch, A.: Characteristics and robustness of Agulhas leakage estimates: an inter-
655   comparison study of Lagrangian methods, Ocean Science, 17, 1067–1080, 2021.

Schott, F. A., Fischer, J., Dengler, M., and Zantopp, R.: Variability of the deep western boundary current east of the Grand Banks, Geophysical Research Letters, 33, 2006.

Sidorenko, D., Danilov, S., Fofonova, V., Cabos, W., Koldunov, N., Scholz, P., Sein, D. V., and Wang, Q.: AMOC, Water Mass Transformations, and Their Responses to Changing Resolution in the Finite-VolumE Sea Ice-Ocean Model, Journal of Advances in Modeling Earth
660   Systems, 12, https://doi.org/https://doi.org/10.1029/2020MS002317, 2020.

Spall, M. A.: Large-Scale Circulations Forced by Localized Mixing over a Sloping Bottom, Journal of Physical Oceanography, 31, https://doi.org/10.1175/1520-0485(2001)031<2369:LSCFBL>2.0.CO;2, 2001.

Spall, M. A.: Boundary currents and watermass transformation in marginal seas, Journal of physical oceanography, 34, 1197–1213, 2004.

Spall, M. A. and Pickart, R. S.: Wind-driven recirculations and exchange in the Labrador and Irminger Seas, Journal of Physical Oceanogra-
665   phy, 33, 1829–1845, 2003.

Straneo, F.: On the connection between dense water formation, overturning, and poleward heat transport in a convective basin, Journal of physical oceanography, 36, 1822–1840, 2006.

Tsujino, H., Urakawa, S., Nakano, H., Small, R. J., Kim, W. M., Yeager, S. G., Danabasoglu, G., Suzuki, T., Bamber, J. L., Bentsen, M., Böning, C. W., Bozec, A., Chassignet, E. P., Curchitser, E., Boeira Dias, F., Durack, P. J., Griffies, S. M., Harada, Y., Ilicak, M., Josey, S. A., Kobayashi, C., Kobayashi, S., Komuro, Y., Large, W. G., Le Sommer, J., Marsland, S. J., Masina, S., Scheinert, M., Tomita, H., Valdivieso, M., and Yamazaki, D.: JRA-55 based surface dataset for driving ocean–sea-ice models (JRA55-do), Ocean Modelling, 130, 79–139, https://doi.org/https://doi.org/10.1016/j.ocemod.2018.07.002, 2018.

Våge, K., Pickart, R. S., Moore, G. W. K., and Ribergaard, M. H.: Winter mixed layer development in the central Irminger Sea: The effect of strong, intermittent wind events, Journal of Physical Oceanography, 38, 541–565, 2008.

Våge, K., Pickart, R. S., Thierry, V., Reverdin, G., Lee, C. M., Petrie, B., Agnew, T. A., Wong, A., and Ribergaard, M. H.: Surprising return of deep convection to the subpolar North Atlantic Ocean in winter 2007–2008, Nature Geoscience, 2, 67–72, 2009.

van Sebille, E., Griffies, S. M., Abernathey, R., Adams, T. P., Berloff, P., Biastoch, A., Blanke, B., Chassignet, E. P., Cheng, Y., Cotter, C. J., et al.: Lagrangian ocean analysis: fundamentals and practices, Ocean Modelling, 2017.

Walin, G.: On the relation between sea-surface heat flow and thermal circulation in the ocean, Tellus, 34, 187–195, 1982.

Waterhouse, A. F., MacKinnon, J. A., Nash, J. D., Alford, M. H., Kunze, E., Simmons, H. L., Polzin, K. L., Laurent, L. C. S., Sun, O. M., Pinkel, R., Talley, L. D., Whalen, C. B., Huussen, T. N., Carter, G. S., Fer, I., Waterman, S., Garabato, A. C. N., Sanford, T. B., and Lee, C. M.: Global Patterns of Diapycnal Mixing from Measurements of the Turbulent Dissipation Rate, Journal of Physical Oceanography, 44, 1854–1872, https://doi.org/10.1175/JPO-D-13-0104.1, 2014.

Xu, X., Schmitz W., J., Hurlburt H., E., Hogan P., J., and Chassignet E., P.: Transport of Nordic Seas overflow water into and within the Irminger Sea: An eddy-resolving simulation and observations, J. Geophys. Res., 115, https://doi.org/10.1029/2010jc006351, 2010.

Xu, X., Rhines, P. B., and Chassignet, E. P.: On mapping the diapycnal water mass transformation of the upper North Atlantic Ocean, Journal of Physical Oceanography, 48, 2233–2258, 2018.

Yashayaev, I. and Loder, J. W.: Recurrent replenishment of Labrador Sea Water and associated decadal scale variability, Journal of Geophysical Research: Oceans, 2016.

Yashayaev, I., Holliday, N. P., Bersch, M., and van Aken, H. M.: The History of the Labrador Sea Water: Production, Spreading, Transformation and Loss, in: Arctic-Subarctic Ocean Fluxes: Defining the Role of the Northern Seas in Climate, pp. 569–612, Springer Netherlands, Dordrecht, https://doi.org/10.1007/978-1-4020-6774-7_25, 2008.

Zantopp, R., Fischer, J., Visbeck, M., and Karstensen, J.: From interannual to decadal—17 years of boundary current transports at the exit of the Labrador Sea, Journal of Geophysical Research: Oceans, 2017.

Zhang, R., Sutton, R., Danabasoglu, G., Kwon, Y., Marsh, R., Yeager, S. G., Amrhein, D. E., and Little, C. M.: A review of the role of the Atlantic Meridional Overturning Circulation in Atlantic multidecadal variability and associated climate impacts, Reviews of Geophysics, 57, 316–375, 2019.

Zou, S. and Lozier, M. S.: Breaking the Linkage Between Labrador Sea Water Production and Its Advective Export to the Subtropical Gyre, J. Phys. Oceanogr., 46, 2169–2182, https://doi.org/10.1175/jpo-d-15-0210.1, 2016.

Zou, S., Bower, A. S., Furey, H., Lozier, S. M., and Xu, X.: Redrawing the Iceland-Scotland Overflow Water pathways in the North Atlantic, Nature Communications, 11, 1890, https://doi.org/10.1038/s41467-020-15513-4, 2020a.

Zou, S., Lozier, M. S., and Xu, X.: Latitudinal Structure of the Meridional Overturning Circulation Variability on interannual to decadal time scales in the North Atlantic Ocean, J. Climate, https://doi.org/10.1175/jcli-d-19-0215.1, 2020b.

Zou, S., Bower, A. S., Furey, H., Pickart, R. S., Houpert, L., and Holliday, N. P.: Observed Deep Cyclonic Eddies around Southern Greenland, Journal of Physical Oceanography, 51, 3235–3252, 2021.

705   Østerhus, S., Turrell, W. R., Hansen, B., Lundberg, P., and Buch, E.: Observed transport estimates between the North Atlantic and the Arctic Mediterranean in the Iceland–Scotland region, Polar Research, 20, 169–175, 2001.